

AD-A253 683



WL-TR-91-4059

OXYGEN BARRIER OXIDES



Rheal Turcotte, Doreen Edwards, Jill Jonkouski  
BIRL, Northwestern University  
1801 Maple Avenue  
Evanston, IL 60201-3135

March 1992

DTIC  
ELECTE  
JUL 31 1992  
S A D

Final Report for Period June 1989 - October 1990

Approved for public release; distribution unlimited

Materials Directorate  
WRIGHT LABORATORY  
AIR FORCE SYSTEMS COMMAND  
WRIGHT PATTERSON AIR FORCE BASE, OH 45433-6533

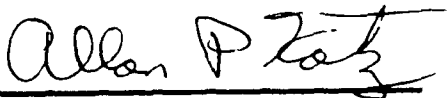
92-20544

## NOTICE

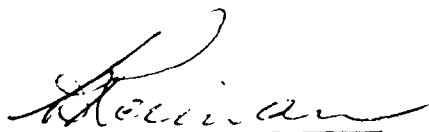
WHEN GOVERNMENT DRAWINGS, SPECIFICATIONS, OR OTHER DATA ARE USED FOR ANY PURPOSE OTHER THAN IN CONNECTION WITH A DEFINITELY GOVERNMENT-RELATED PROCUREMENT, THE UNITED STATES GOVERNMENT INCURS NO RESPONSIBILITY OR ANY OBLIGATION WHATSOEVER. THE FACT THAT THE GOVERNMENT MAY HAVE FORMULATED OR IN ANY WAY SUPPLIED THE SAID DRAWINGS, SPECIFICATIONS, OR OTHER DATA, IS NOT TO BE REGARDED BY IMPLICATION, OR OTHERWISE IN ANY MANNER CONSTRUED, AS LICENSING THE HOLDER, OR ANY OTHER PERSON OR CORPORATION; OR AS CONVEYING ANY RIGHTS OR PERMISSION TO MANUFACTURE, USE, OR SELL ANY PATENTED INVENTION THAT MAY IN ANY WAY BE RELATED THERETO.

THIS REPORT HAS BEEN REVIEWED BY THE OFFICE OF PUBLIC AFFAIRS (ASD/PA) AND IS RELEASABLE TO THE NATIONAL TECHNICAL INFORMATION SERVICE (NTIS). AT NTIS IT WILL BE AVAILABLE TO THE GENERAL PUBLIC INCLUDING FOREIGN NATIONS.

THIS TECHNICAL REPORT HAS BEEN REVIEWED AND IS APPROVED FOR PUBLICATION.



ALLAN P. KATZ, Project Engineer



WALTER H. REIMANN  
Chief, Materials Development Branch  
Materials Directorate

IF YOUR ADDRESS HAS CHANGED, IF YOU WISH TO BE REMOVED FROM OUR MAILING LIST, OR IF THE ADDRESSEE IS NO LONGER EMPLOYED BY YOUR ORGANIZATION PLEASE NOTIFY W4/M4411, WRIGHT-PATTERSON AFB, OH 45433-6503 TO HELP MAINTAIN A CURRENT MAILING LIST.

COPIES OF THIS REPORT SHOULD NOT BE RETURNED UNLESS RETURN IS REQUIRED BY SECURITY CONSIDERATIONS, CONTRACTUAL OBLIGATIONS, OR NOTICE ON A SPECIFIC DOCUMENT.

REPORT DOCUMENTATION PAGE			Form Approved OMB No. 0704-0188	
<small>Public burden for this collection of information is estimated to average 1 hour per response, including the time for reviewing instructions, searching existing data sources, gathering and maintaining the data needed, and completing and reviewing the collection of information. Send comments regarding this burden estimate or any other aspect of this collection of information, including suggestions for reducing this burden, to Washington Headquarters Services, Directorate for Information Operations and Reports, 1215 Jefferson Davis Highway, Suite 1204, Arlington, VA 22202-4302, and to the Office of Management and Budget, Paperwork Reduction Project (0704-0188), Washington, DC 20503.</small>				
1. AGENCY USE ONLY (Leave blank)		2. REPORT DATE March 1992		3. REPORT TYPE AND DATES COVERED Final Report June - October 1990
4. TITLE AND SUBTITLE  Oxygen Barrier Oxides			5. FUNDING NUMBERS C: F33615-87-C-5339 PE:62102F PR:2420 TA:01 WV:AH	
6. AUTHOR(S) Rheal Turcotte Doreen Edwards Jill Jonkouski				
7. PERFORMING ORGANIZATION NAME(S) AND ADDRESS(ES) BIRL Northwestern University 1801 Maple Avenue Evanston, IL 60201-3135			8. PERFORMING ORGANIZATION REPORT NUMBER  A-400	
9. SPONSORING / MONITORING AGENCY NAME(S) AND ADDRESS(ES) Dr. Allan Katz (513) 255-9824 Wright Laboratory Materials Directorate (WL/MLLM) Wright Patterson AFB, OH 45433-6533			10. SPONSORING / MONITORING AGENCY REPORT NUMBER  WL-TR-91-4059	
11. SUPPLEMENTARY NOTES				
12a. DISTRIBUTION / AVAILABILITY STATEMENT  Approved for public release, distribution unlimited			12b. DISTRIBUTION CODE	
13. ABSTRACT (Maximum 200 words) A series of mixed oxides with composition $Zr_3M_4O_{12}$ were prepared as candidate high-melting-point ceramics for composite applications. The oxides selected should have significantly reduced oxygen diffusion coefficients compared to cubic-stabilized zirconia. Colloidal processing and conventional sintering produced samples with densities near 98% of theoretical. $Zr_3M_4O_{12}$ compositions with $M = Sc, Y, La, \text{ and } Gd$ , as well as $Y_2O_3$ and cubic-stabilized zirconia, were studied using the $^{18}O$ -exchange method to measure diffusivity in the range $900^\circ - 1200^\circ C$ .  The materials span about three orders of magnitude in diffusivity, with $D$ ranging from $10^{-7}$ to $10^{-10} \text{ cm}^2/\text{s}$ at $1135^\circ C$ . $Zr_3Sc_4O_{12}$ and $Y_2O_3$ were found to have the lowest diffusivity, and the temperature dependence for all of the rare earth containing ceramics was similar. For the mixed oxides, there is no apparent trend correlating diffusivity and the crystal lattice dimensions. Porous microstructures in some of the materials, especially cubic- $ZrO_2$ and $Zr_3Gd_4O_{12}$ , led to experimental $^{18}O$ -exchange versus time curves which could not be easily fit to theoretical curves. Doping studies of $Sc^{3+}$ and $Ta^{5+}$ in $Zr_3La_4O_{12}$ showed no significant effect on diffusivity at $1135^\circ C$ .				
14. SUBJECT TERMS  Oxide ceramics, oxygen diffusion, zirconia			15. NUMBER OF PAGES	
			16. PRICE CODE	
17. SECURITY CLASSIFICATION OF REPORT Unclassified	18. SECURITY CLASSIFICATION OF THIS PAGE Unclassified	19. SECURITY CLASSIFICATION OF ABSTRACT Unclassified	20. LIMITATION OF ABSTRACT  Unlimited	

## TABLE OF CONTENTS

ACKNOWLEDGEMENTS . . . . .	v
SUMMARY . . . . .	1
INTRODUCTION . . . . .	2
EXPERIMENTAL PROCEDURES . . . . .	3
Sample Preparation . . . . .	3
Diffusivity Measurements . . . . .	5
Apparatus . . . . .	6
Experimental Technique . . . . .	8
Diffusion Calculations . . . . .	12
RESULTS . . . . .	12
Sample Characterization . . . . .	12
Electron Microscopy Examination . . . . .	12
X-Ray Diffraction Results . . . . .	14
Diffusion Results . . . . .	17
RELATED WORK . . . . .	22
CONCLUSIONS . . . . .	24
REFERENCES . . . . .	25
APPENDIX A PRELIMINARY PROCESSING . . . . .	A-1
Coprecipitation and Pressureless Sintering . . . . .	A-1
Coprecipitation and Hot Pressing . . . . .	A-6
Coprecipitation with Dispersant and Pressureless Sintering . . . . .	A-10
APPENDIX B THERMOGRAMS OF STARTING MATERIALS . . . . .	B-1
APPENDIX C COMPUTER PROGRAM FOR CALCULATING THEORETICAL CURVES . . . . .	C-1
APPENDIX D SCANNING ELECTRON MICROGRAPHS . . . . .	D-1
APPENDIX E X-RAY DIFFRACTION PATTERNS . . . . .	E-1
APPENDIX F [ <sup>18</sup> O] VS TIME DATA COMPARED TO THEORETICAL CURVES . . . . .	F-1

## LIST OF FIGURES

FIGURE 1.	Schematic of Diffusion Apparatus . . . . .	7
FIGURE 2.	Mass Spectrometer Response for Decomposition of $\text{CaCO}_3$ . . . .	9
FIGURE 3.	Typical Experimental Run Results . . . . .	11
FIGURE 4.	Lattice Parameter Versus Cation Radii . . . . .	16
FIGURE 5.	$[\text{}^{18}\text{O}]$ Versus Time for $\text{Zr}_3\text{Sc}_4\text{O}_{12}$ at $1135^\circ\text{C}$ . . . . .	18
FIGURE 6.	Temperature Dependence of Oxygen Diffusivity . . . . .	20
FIGURE 7.	Comparison of Oxygen Diffusivity of Related Oxides (--- this study, ____ literature) . . . . .	23
FIGURE A.1.	Effect of Prefiring Temperature on Fired Pellet Density .	A-5
FIGURE A.2.	Micrograph of "As Hot-Pressed" $\text{Zr}_3\text{Y}_4\text{O}_{12}$ . . . . .	A-8
FIGURE A.3.	Micrograph of $\text{Zr}_3\text{Y}_4\text{O}_{12}$ After Oxidation . . . . .	A-8
FIGURE A.4.	Micrograph of $\text{Zr}_3\text{Y}_4\text{O}_{12}$ After Anneal . . . . .	A-9
FIGURE B.1.	Thermogram for Scandium Nitrate Tetrahydrate . . . . .	B-1
FIGURE B.2.	Thermogram for Yttrium Nitrate Hexahydrate . . . . .	B-1
FIGURE B.3.	Thermogram for Lanthanum Nitrate Hexahydrate . . . . .	B-2
FIGURE B.4.	Thermogram for Gadolinium Nitrate Pentahydrate . . . . .	B-2
FIGURE B.5.	Thermogram for Zirconyl Nitrate . . . . .	B-3
FIGURE B.6.	Thermogram for Darvan C, an Ammonium Polymethacrylate Additive . . . . .	B-3
FIGURE D.1.	Scanning Electron Micrograph of $\text{Zr}_3\text{Sc}_4\text{O}_{12}$ . . . . .	D-1
FIGURE D.2.	Scanning Electron Micrograph of $\text{Zr}_3\text{Sc}_4\text{O}_{12}$ . . . . .	D-1
FIGURE D.3.	Scanning Electron Micrograph of $\text{Zr}_3\text{Y}_4\text{O}_{12}$ . . . . .	D-2
FIGURE D.4.	Scanning Electron Micrograph of $\text{Zr}_3\text{Y}_4\text{O}_{12}$ . . . . .	D-2
FIGURE D.5.	Scanning Electron Micrograph of $\text{Zr}_3\text{La}_4\text{O}_{12}$ . . . . .	D-3
FIGURE D.6.	Scanning Electron Micrograph of $\text{Zr}_3\text{La}_4\text{O}_{12}$ . . . . .	D-3
FIGURE D.7.	Scanning Electron Micrograph of $\text{Zr}_{2.98}\text{Sc}_{0.01}\text{Ta}_{0.01}\text{La}_4\text{O}_{12}$ . . .	D-4
FIGURE D.8.	Scanning Electron Micrograph of $\text{Zr}_{2.9}\text{Sc}_{0.05}\text{Ta}_{0.05}\text{La}_4\text{O}_{12}$ . . .	D-4
FIGURE D.9.	Scanning Electron Micrograph of $\text{Zr}_{2.7}\text{Sc}_{0.15}\text{Ta}_{0.15}\text{La}_4\text{O}_{12}$ . . .	D-5

# LIST OF FIGURES (cont'd)

FIGURE D.10. Scanning Electron Micrograph of $Zr_3La_{3.8}Sc_{0.2}O_{12}$ . . . . .	D-5
FIGURE D.11. Scanning Electron Micrograph of $Zr_3Gd_4O_{12}$ . . . . .	D-6
FIGURE D.12. Scanning Electron Micrograph of $Zr_3Gd_4O_{12}$ . . . . .	D-6
FIGURE D.13. Scanning Electron Micrograph of $Y_2O_3$ . . . . .	D-7
FIGURE D.14. Scanning Electron Micrograph of Cubic Zirconia (CZ101) . .	D-7
FIGURE E.1. X-ray Diffraction pattern for $Zr_3Sc_4O_{12}$ (hexagonal) . . . .	E-2
FIGURE E.2. X-ray Diffraction Pattern for $Zr_3Y_4O_{12}$ (cubic) . . . . .	E-3
FIGURE E.3. X-ray Diffraction Pattern for $Zr_3La_4O_{12}$ (cubic) . . . . .	E-4
FIGURE E.4. X-ray Diffraction Pattern for $Zr_3La_3Sc_{0.2}O_{12}$ (cubic) . . .	E-5
FIGURE E.5. X-ray Diffraction Pattern for $Zr_3Gd_4O_{12}$ (cubic) . . . . .	E-6
FIGURE E.6. X-ray Diffraction Pattern for CZ101 (cubic) . . . . .	E-7
FIGURE F.1. $[^{18}O]$ vs Time Curve for $Zr_3Sc_4O_{12}$ at 1135°C . . . . .	F-1
FIGURE F.2. $[^{18}O]$ vs Time Curve for $Zr_3Sc_4O_{12}$ at 1080°C . . . . .	F-2
FIGURE F.3. $[^{18}O]$ vs Time Curve for $Zr_3Sc_4O_{12}$ at 975°C . . . . .	F-3
FIGURE F.4. $[^{18}O]$ vs Time Curve for $Zr_3Y_4O_{12}$ at 1135°C . . . . .	F-4
FIGURE F.5. $[^{18}O]$ vs Time Curve for $Zr_3La_4O_{12}$ at 1135°C . . . . .	F-5
FIGURE F.6. $[^{18}O]$ vs Time Curve for $Zr_{2.98}Sc_{.01}La_4O_{12}$ at 1135°C . . . .	F-6
FIGURE F.7. $[^{18}O]$ vs Time Curve for $Zr_{2.9}Sc_{.05}Ta_{.05}La_4O_{12}$ at 1135°C . . .	F-7
FIGURE F.8. $[^{18}O]$ vs Time Curve for $Zr_{2.7}Sc_{.15}Ta_{.15}La_4O_{12}$ at 1135°C . . .	F-8
FIGURE F.9. $[^{18}O]$ vs Time Curve for $Zr_3La_{3.8}Sc_{.2}O_{12}$ at 1135°C . . . . .	F-9
FIGURE F.10. $[^{18}O]$ vs Time Curve for $Zr_3Gd_4O_{12}$ at 1135°C . . . . .	F-10
FIGURE F.11. $[^{18}O]$ vs Time Curve for Cubic Zirconia (CZ101) . . . . .	F-11
FIGURE F.12. $[^{18}O]$ vs Time Curve for at $Y_2O_3$ at 1135°C . . . . .	F-12
FIGURE F.13. $[^{18}O]$ vs Time Curve for $Y_2O_3$ at 1080°C . . . . .	F-13
FIGURE F.14. $[^{18}O]$ vs Time Curve for $Y_2O_3$ at 975°C . . . . .	F-14

## LIST OF TABLES

TABLE 1.	Densities and Lattice Parameters of Diffusion Samples . . . .	5
TABLE 2.	Measured Diffusion Coefficients . . . . .	21
TABLE 3.	Activation Energies and $D_0$ for Undoped Materials . . . . .	22
TABLE A.1.	Processing Conditions . . . . .	A-3
TABLE A.2.	Density of $Zr_3Y_4O_{12}$ Prepared with Additives . . . . .	A-4
TABLE A.3.	Densities of Hot-Pressed Material . . . . .	A-6
TABLE A.4.	Densities of Materials Prepared with Dispersant . . . . .	A-11
TABLE A.5.	Densities of Materials with Post-Calcine Processing . . . .	A-12

### ACKNOWLEDGEMENTS

The authors wish to acknowledge the assistance provided by Fariha Feroz and Brooke Faire in preparation of samples and collection of data. We also wish to thank Paul Rudnik who performed final X-ray analysis of the materials, and Betty Williams Burns who provided much assistance in the preparation of this final document.

We also wish to thank the Air Force Materials Directorate/Wright Laboratory for their support of this project.

Accession For	
NTIS CRA&I	<input checked="checked" type="checkbox"/>
DTIC TAB	<input type="checkbox"/>
Unannounced	<input type="checkbox"/>
Justification	
By	
Distribution /	
Availability Codes	
Dist	Avail and/or Special
A-1	

DTIC QUALITY INSPECTED 2



## SUMMARY

Based on thermodynamic stability and crystal structure considerations, a series of mixed oxides with composition  $Zr_3M_4O_{12}$  were prepared as candidate high-melting-point ceramics for composite applications. The oxides selected should have significantly reduced oxygen diffusion coefficients compared to cubic-stabilized zirconia. Colloidal processing and conventional sintering produced samples with densities near 98% of theoretical.  $Zr_3M_4O_{12}$  compositions with  $M = Sc, Y, La,$  and  $Gd$ , as well as  $Y_2O_3$  and cubic-stabilized zirconia, were studied using the  $^{18}O$ -exchange method to measure diffusivity in the range  $900^{\circ}$ - $1200^{\circ}C$ .

The materials span about three orders of magnitude in diffusivity, with  $D$  ranging from  $10^{-7}$  to  $10^{-10}$   $cm^2/s$  at  $1135^{\circ}C$ .  $Zr_3Sc_4O_{12}$  and  $Y_2O_3$  were found to have the lowest diffusivity, and the temperature dependence for all of the rare earth containing ceramics was similar. For the mixed oxides, there is no apparent trend correlating diffusivity and the crystal lattice dimensions. Porous microstructures in some of the materials, especially cubic- $ZrO_2$  and  $Zr_3Gd_4O_{12}$ , led to experimental  $^{18}O$ -exchange versus time curves which could not be easily fitted to theoretical curves. Doping studies of  $Sc^{3+}$  and  $Ta^{5+}$  in  $Zr_3La_4O_{12}$  showed no significant effect on diffusivity at  $1135^{\circ}C$ .

Based on this study and other complications concerning altermixing oxides, pure  $Y_2O_3$  is considered the most attractive material evaluated.

## INTRODUCTION

The development of advanced turbine engines may require use of new ceramic-oxide based composites or new oxide coatings. These materials must have low oxygen diffusivities to protect oxidizable components, such as carbon fibers, while remaining thermochemically inert at as high a temperature as possible.

This study involved preparation of several zirconia-based ceramics and measurement of their oxygen diffusion characteristics. Based on thermodynamic and structural considerations, modifications of fluorite-related oxides of the composition  $Zr_3M_4O_{12}$  were chosen as promising candidates, where M is yttrium, scandium, lanthanum, or gadolinium. The  $M_7O_{12}$  compositions have melting points above 2500°C. By creation of the ordered crystal structure corresponding to this composition, along with control of oxygen vacancy defects, the potential exists to reduce diffusion coefficients several orders of magnitude by comparison to cubic-stabilized zirconia. The objective of this study was to evaluate the degree to which diffusivity could be reduced, using a mass spectrometer -  $^{18}O$  exchange method to measure diffusivity as a function of temperature.

The report is structured into sections summarizing the experimental approach and final results, followed by a series of appendices containing supporting experimental data.

## EXPERIMENTAL PROCEDURES

### Sample Preparation

The mixed oxides were prepared by hydroxide precipitation from nitrate solutions, followed by calcination and conventional sintering. A significant effort was required to develop procedures which eventually produced high density, homogeneous ceramics. Appendix A summarizes results of the preliminary fabrication effort, including an unsuccessful attempt to hot press the materials. In this section, we provide details of the final successful preparation "recipe," which we believe will be broadly useful for preparation of related mixed oxides.

The ceramics studied were prepared by a variant of traditional coprecipitation, powder calcination, cold pressing, and sintering, giving a homogeneous product near 98% of theoretical density. The starting materials were nitrate salts with a stated purity of 99.9%. Thermogravimetric analysis, shown in Appendix B, Figures B.1 - B.6, was used to determine precise metal content since most of the salts used are hygroscopic and rarely stoichiometric with respect to water of hydration. For the Zr/La, Zr/Gd, and Zr/Y compositions, nitrate salts were dissolved in water at 40°C to make a solution that was 0.150 molar with respect to the zirconium cation and 0.200 molar with respect to La, Gd, or Y. For the Zr/Sc composition, more water was required for complete dissolution of the nitrate salts, resulting in a solution that was 0.100 molar with respect to zirconium and 0.133 molar with respect to scandium. Both preparations gave the final oxide composition of  $Zr_3M_4O_{12}$ .

Each nitrate solution was cooled to room temperature and added with rapid mixing to a 3 molar solution of ammonium hydroxide, containing a commercially available surfactant (Darvan C). The amount of ammonium hydroxide used was in 66% excess of the amount required to react with the nitrates, and Darvan C was added as 5 weight percent of the theoretical oxide ( $Zr_3M_4O_{12}$ ) yield. The hydroxide products were blended for 5 to 10 minutes, then dried at 100°C in air, in teflon beakers. While the ultimate stability of the colloidal suspension is not known, a covered sample of the Zr/Y suspension showed no separation after 6 weeks of storage.

After overnight drying, the product was crushed with a mortar and pestle, then calcined to 650°C for one hour, which was sufficient to completely vaporize the Darvan C as demonstrated by the thermogram in Figure B.6. The calcined powders were crushed with a mortar and pestle, heated to 1600°C at 5°C/minute, and held for 30 minutes before cooling at 10°-20°C/minute. The prefired powders (60% by weight) were then mixed with toluene (40% by weight) and ball milled for 24 hours in 60 ml polyethylene bottles which were approximately half filled with 1/4 inch zirconia grinding media. (All of the individual preparations were at a scale giving 10-20 grams of product.)

The slurries were removed from the zirconia media and dried in air at 100°C. The dried powders were crushed in a mortar and pestle and cold pressed in a 1/2 inch diameter die at pressures near 40,000 psi. The green pellets were then fired in yttria-stabilized zirconia crucibles at 1680°C for 6 hours. Sintered pellets of the  $Zr_3Y_4O_{12}$  and  $Zr_3Gd_4O_{12}$  were cream colored. The  $Zr_3Sc_4O_{12}$  pellets were white, and the  $Zr_3La_4O_{12}$  pellets were olive-green.

Four samples of  $Zr_3La_4O_{12}$ , doped with scandium and a combination of scandium and tantalum, were prepared. In one sample,  $Sc^{3+}$  was added to replace 5% of the lanthanum cations. In the other three materials,  $Sc^{3+}$  was added to replace 0.33, 1.67, and 5.0% of the zirconium cations, with  $Ta^{5+}$  added to replace an additional 0.33, 1.67, and 5.0% of the zirconium atoms to maintain the oxygen/metal stoichiometry. These materials were prepared in the same manner as the undoped samples. Scandium nitrate was dissolved with the other nitrates. Tantalum, however, has no soluble salts and was added as  $Ta_2O_5$  to the ammonium hydroxide, containing the dispersant, to facilitate as even a distribution as possible. Like the undoped  $Zr_3La_4O_{12}$ , the doped materials were also olive-green after sintering.

The final pellet geometry was a disc 10mm in diameter with thickness about 2 mm. The  $ZrO_2$  reference material\* was cut from a rod to a disc approximately 1 mm thick.

\*Ceramtec CZ101 - supplied by E. L. Courtright, Battelle Pacific Northwest Laboratories.

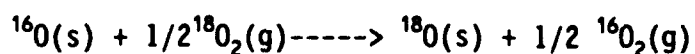
The densities of the ten materials used in the diffusion experiments are given in Table 1. Archimedes' method was used to determine the actual densities. The theoretical densities shown were calculated using measured lattice parameters and assuming a fluorite-cubic solid solution.

TABLE 1. Densities and Lattice Parameters of Diffusion Samples

Composition	Density (% theory)	Open Porosity (%)	Lattice Parameter (Å)	Theo- retical Density (g/cm <sup>3</sup> )
Zr <sub>3</sub> Sc <sub>4</sub> O <sub>12</sub>	98.9%	0.84%	5.026	4.825
Zr <sub>3</sub> Y <sub>4</sub> O <sub>12</sub>	97.2%	0.91%	5.222	5.472
Zr <sub>3</sub> Gd <sub>4</sub> O <sub>12</sub>	94.0%	1.50%	5.289	7.019
Zr <sub>3</sub> La <sub>4</sub> O <sub>12</sub>	97.6%	0.75%	5.413	6.109
Zr <sub>2.98</sub> Sc <sub>0.01</sub> Ta <sub>0.01</sub> La <sub>4</sub> O <sub>12</sub>	98.9%	0.15%	5.411	6.118
Zr <sub>2.9</sub> Sc <sub>0.05</sub> Ta <sub>0.05</sub> La <sub>4</sub> O <sub>12</sub>	98.0%	0.27%	5.410	6.134
Zr <sub>2.7</sub> Sc <sub>0.15</sub> Ta <sub>0.15</sub> La <sub>4</sub> O <sub>12</sub>	98.4%	1.10%	5.419	6.127
Zr <sub>3</sub> La <sub>3.8</sub> Sc <sub>0.2</sub> O <sub>12</sub>	99.1%	0.39%	5.412	5.998
Y <sub>2</sub> O <sub>3</sub>	97.0%	0.41%	5.015	
6ZrO <sub>3</sub> (Cubic stabilized Zirconia)	-----	-----	5.140	-----

#### Diffusivity Measurements

The oxygen diffusivity was determined using an oxygen exchange/mass spectrometric technique. In this method, the samples were placed in an <sup>18</sup>O-enriched atmosphere at elevated temperatures. Atomic exchange occurs, limited by the rate of oxygen transport in the solid, as follows:



The mass spectrometer monitored the composition of the gas as the  $^{18}\text{O}$  decreased and  $^{16}\text{O}$  increased to an equilibrium composition. As discussed later in this section, under appropriate experimental conditions, the mathematics of this process are well understood theoretically. By comparison of the experimental gas composition-versus-time curve to theoretical curves, the diffusion coefficient can be easily estimated. There is a fundamental assumption in this approach that the gas/solid surface equilibrium step is rapid compared to diffusion in the solid. The final results do justify this assumption.

### Apparatus

Figure 1 is a schematic of the diffusion apparatus. A turbo-molecular pump evacuated the system, and a gas manifold regulated the incoming gases. Due to the cost of enriched oxygen, its source was situated to allow for the least possible line volume, and it was recovered in a molecular sieve trap. The volume of gas available during the diffusion experiments, that enclosed by  $V_4, V_5, V_6$ , and  $V_8$ , was determined by gas expansion. To accomplish this, the entire system was evacuated and determined to be leak tight. The volume enclosed by  $V_4, V_5, V_6$ , and  $V_7$  was backfilled with argon, and the pressure was recorded. The valve leading to the reaction chamber,  $V_7$ , was then opened, and the new lower pressure was recorded. This experiment was repeated with a steel cylinder of known volume in the main chamber. Using the ideal gas law, the system volume was determined to be 0.462 liters.

Approximately 25% of the experimental volume, that is, the lower part of the quartz tube, was heated by a resistance furnace. The temperature was measured by a type K thermocouple and controlled by a set point temperature controller to  $\pm 2^\circ\text{C}$ . The pressure was monitored by an MKS capacitance manometer. A magnet system lowered and raised the diffusion sample to and from the hot zone.

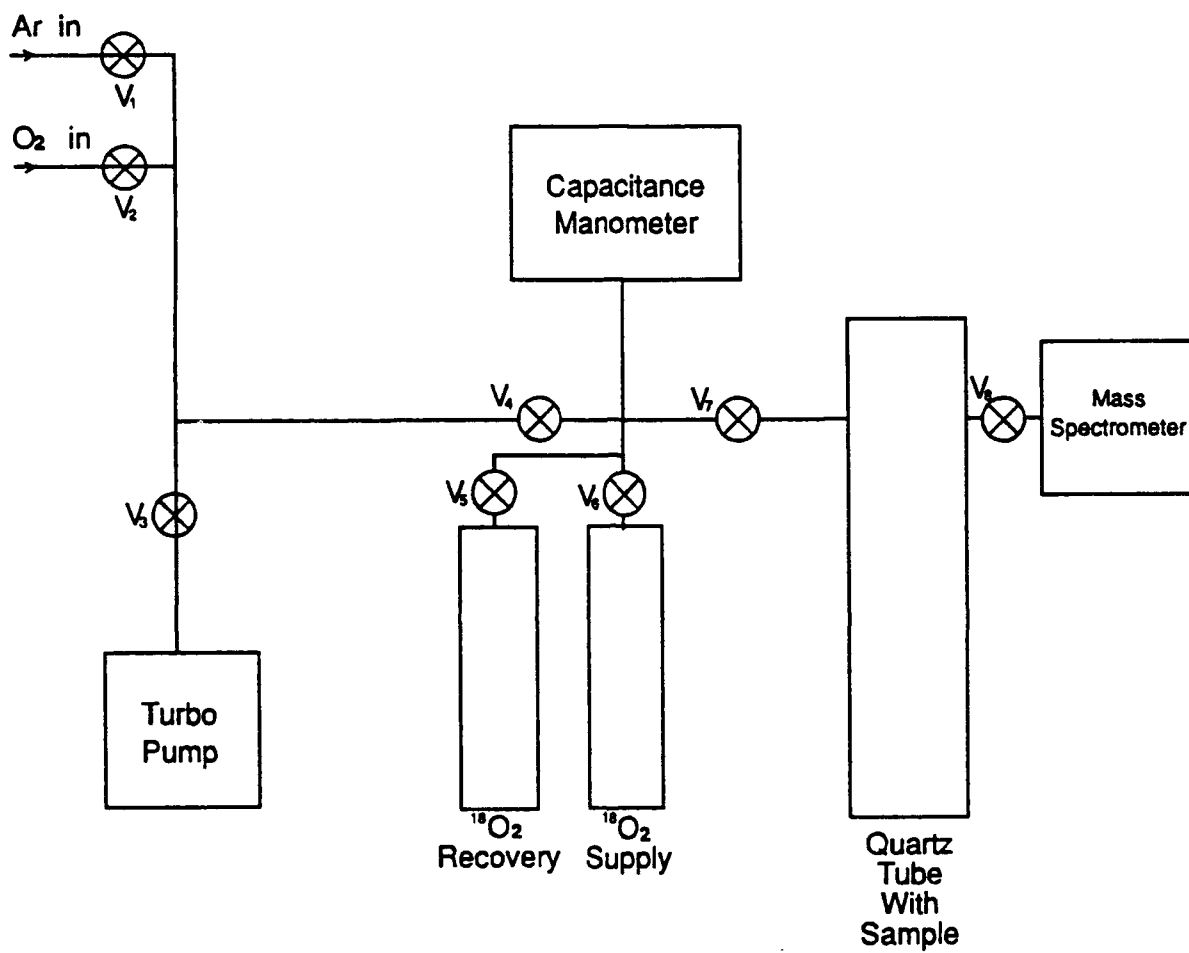


**FIGURE 1. Schematic of Diffusion Apparatus**

An adjustable molecular leak valve,  $V_8$ , led to the quadrupole mass spectrometer. The leak rate was such that the pressure in the diffusion chamber decreased less than 1%/hour and the pressure in the quadrupole mass spectrometer was approximately  $3 \times 10^{-6}$  torr. At an operating pressure of 150-200 torr, the sampling lag time was 1-2 minutes which was considered acceptable for experiments typically 2-8 hours in duration. Data from the mass spectrometer, a Leybold Inficon Quadrex PPC, were collected using Leybold Inficon software and an IBM-XT. One data set was stored every 100-300 seconds, depending upon the duration of the experiment.

To check the response time and linearity of the mass spectrometer system, calcium carbonate was decomposed in an argon atmosphere at a pressure of 145-155 torr. The mass spectrometer signals for carbon dioxide and argon were monitored. After complete decomposition, the argon signals were normalized using the ideal gas law. As shown in Figure 2, the carbon dioxide signal is linearly related to the mass of calcium carbonate decomposed, demonstrating that the system response was linear in the gas concentration range of interest.

### Experimental Technique

Each  $^{18}\text{O}$ -diffusion experiment was conducted in the following manner. The test sample was placed in the test chamber, and the system was evacuated. Once a leak-tight system was confirmed, the test sample was equilibrated in  $^{16}\text{O}_2$  at the chosen test pressure (nominally 150 torr) and test temperature. After a time equal to or exceeding the expected duration of the diffusion experiment, the pellet was removed from the hot zone, and the system was evacuated. The  $^{18}\text{O}$  enriched gas was then admitted, and the system was monitored with the pellet in the cool zone to verify system stability. Once stability was verified, the pellet was lowered into the hot zone. The mass spectrometer/computer monitored the signals of masses 28, 32, 34, and 36 in intervals ranging from 100-300 seconds depending upon the expected duration of the run. Monitoring of nitrogen, mass 28, insured that no unexpected atmospheric leaks in the system would affect the subsequent data analysis.



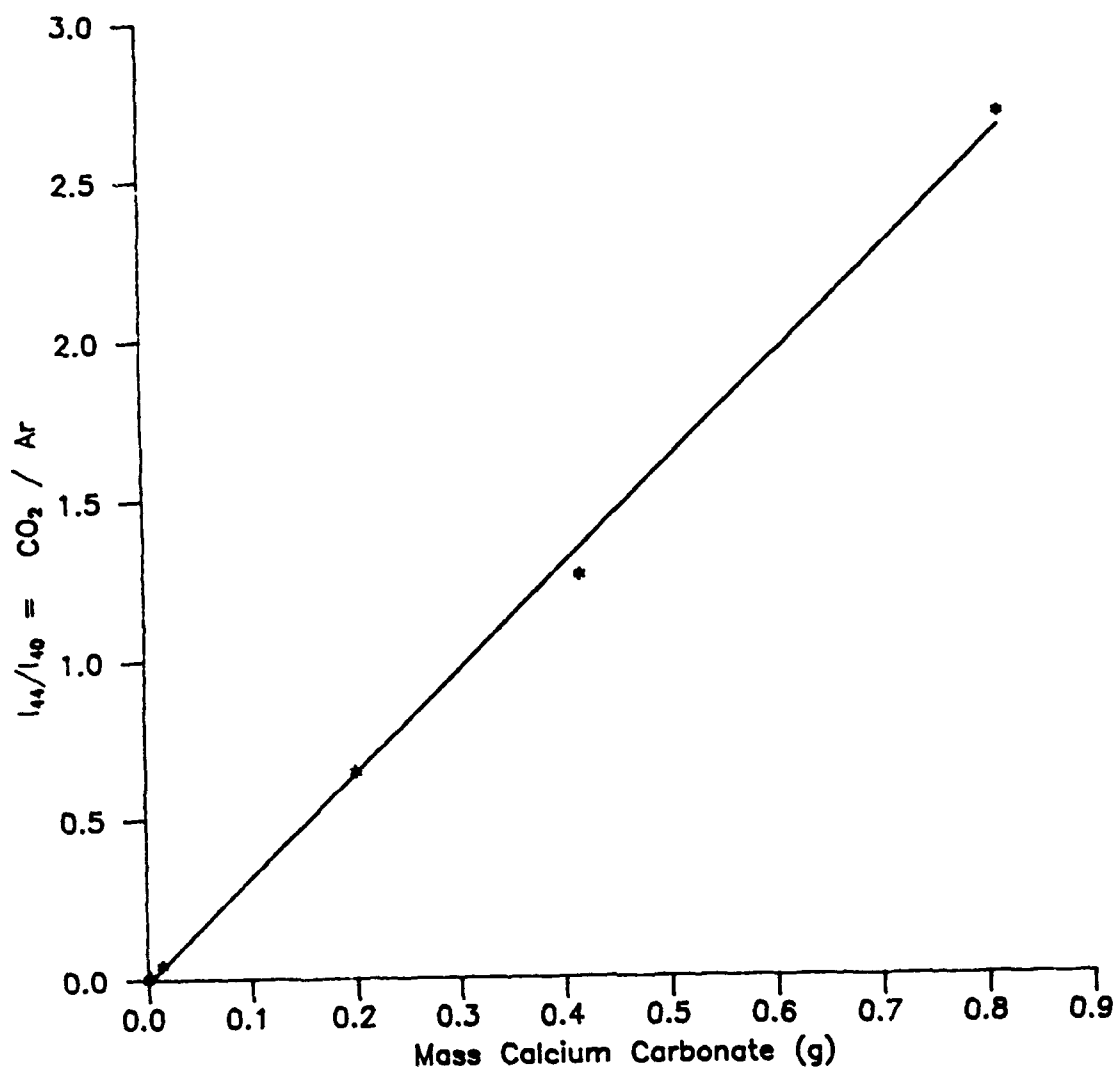


**FIGURE 2. Mass Spectrometer Response for Decomposition of  $\text{CaCO}_3$**

The signals for mass 32, 34, and 36 monitored  $^{16}\text{O}_2$ ,  $^{16}\text{O}^{18}\text{O}$ , and  $^{18}\text{O}_2$ . The fragmentation fraction for each of the oxygen species from diatomic to monatomic gas was assumed to be identical. Therefore, the only correction factors needed were for the varying masses.

By convention, the correction factor for  $\text{N}_2$ , mass 28, is unity. Other signals are corrected as follows:

$$I_{\text{corr}} = I_{\text{meas}}/\text{CF}$$

where  $I_{\text{corr}}$  = corrected signal

$I_{\text{meas}}$  = measured signal

CF = correction factor

= 28/32 for mass 32

= 28/34 for mass 34

= 28/36 for mass 36

The atom fraction of  $^{18}\text{O}$  was then calculated as:

$$[^{18}\text{O}] = \frac{I_{36 \text{ corr}} + 1/2(I_{34 \text{ corr}})}{I_{32 \text{ corr}} + I_{34 \text{ corr}} + I_{36 \text{ corr}}}$$

For all diffusion work reported, nitrogen was monitored, but not detected, and is not included in the equation above.

Figure 3 shows a typical experimental gas concentration versus time curve. Prior to lowering the sample into the hot zone, a slight decrease in the  $^{18}\text{O}$  concentration was detected, presumably due to exchange with the quartz furnace tube. However, this decrease was negligible compared to the decrease during the diffusion run. After the pellet was removed from the hot zone, the  $^{18}\text{O}$  concentration leveled off, indicating continued minimal exchange with the diffusion apparatus.

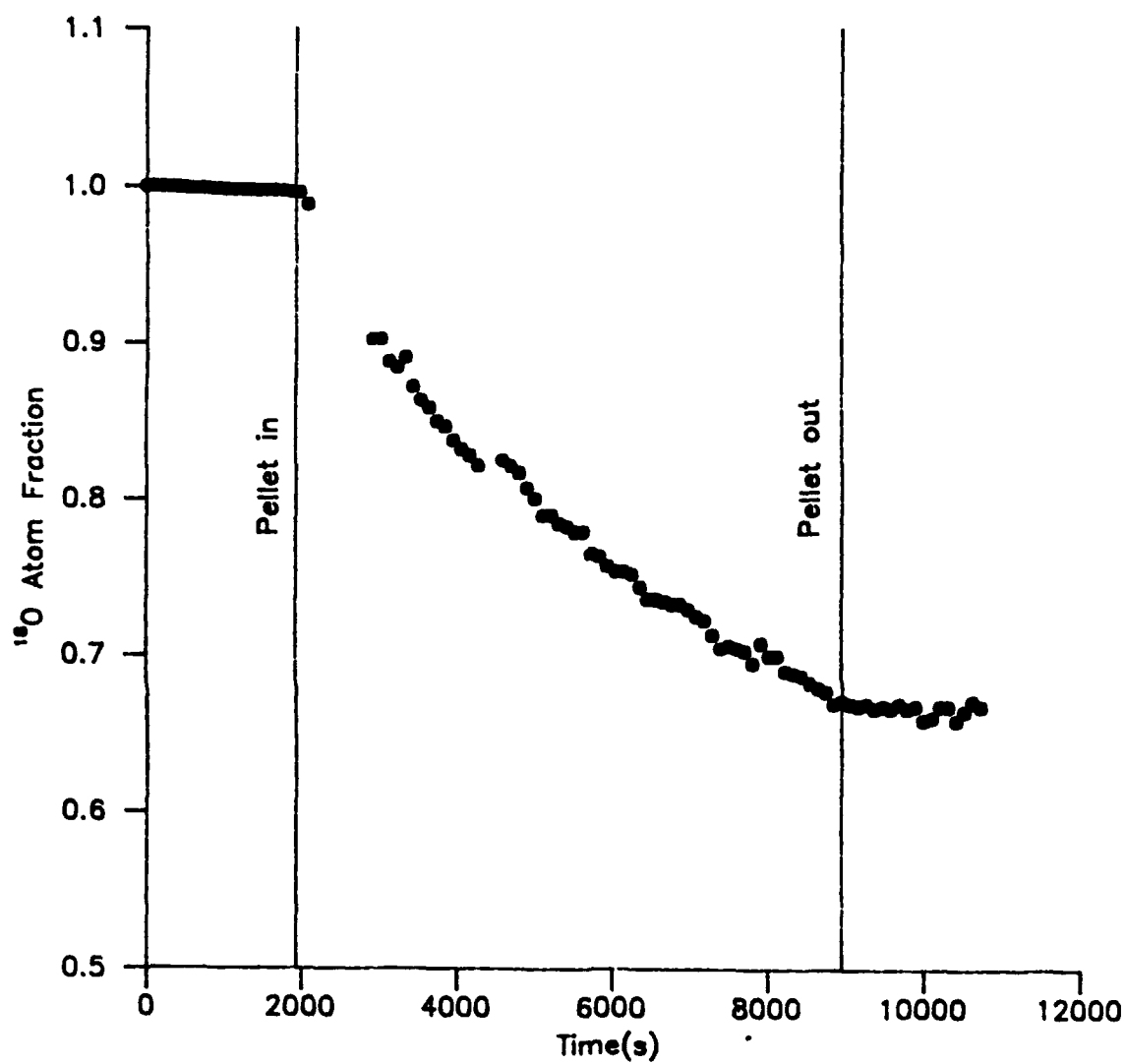


**FIGURE 3. Typical Experimental Run Results**

## Diffusion Calculations

A PC-based computer program solving Fick's second law was written to interpret the diffusion data. The Fortran program is provided in Appendix C. The calculation assumes gas diffusion into an infinite plane from a stirred solution of limited volume. The boundary conditions used to solve Fick's second law equation specify that: 1) the initial  $^{18}\text{O}$  concentration in the solid is 0, and 2) the rate of oxygen removal from the gas is equal to the oxygen uptake in the solid. The diffusion equation is solved via a Laplace transformation expressing  $[^{18}\text{O}_{\text{gas}}]$  in terms of an infinite series. The computer program uses up to 1000 terms to estimate the convergence of the infinite series, introducing less than 0.001% error. Inputs of  $[\text{O}_{\text{gas}}]/[\text{O}_{\text{solid}}]$ , initial  $[^{18}\text{O}_{\text{gas}}]$ , equilibrium  $[^{18}\text{O}]$ ,  $D$ , and sample thickness result in an output of  $[^{18}\text{O}]$  versus time which can be directly compared to experimental data.  $D$  is changed until the best fit is obtained.

A key assumption of the mathematical model is slightly violated in the actual experiment. The mathematical model is based on diffusion into an infinite homogenous plane. In the actual experiment, the samples are not infinite planes, but rather discs about 10mm in diameter and 2mm thick. In a typical experiment with  $D = 1 \times 10^{-8}$  and  $t = 7000\text{s}$ , the penetration depth, approximated by  $(Dt)^{1/2}$ , is  $80\mu\text{m}$ . While this penetration depth leads to negligible overlap of diffusion fields at the edges of the pellet, the diffusion extends through several layers of crystallites, which are less than  $10\mu\text{m}$ . Therefore, the pores and grain boundaries play some role in the diffusion process. As will be seen later, the degree of "fit" between the experimental data and the calculated curves was very good for the most dense samples, but not as good for those with higher porosity.

## RESULTS

### Sample Characterization

#### Electron Microscopy Examination

Representative samples of each of the materials were fractured and coated with 200Å of gold. Appendix D contains SEM micrographs for each of the materials studied, where it is shown that the microstructures are generally similar, but

different in detail. Some specific comments about each of the materials are as follows:

Zr<sub>3</sub>Sc<sub>4</sub>O<sub>12</sub> (D.1 and D.2). The grains appear equiaxed and are typically 5-10um. The closed porosity is minimal, as is expected with material near 99% of theoretical density, and occurs mainly at the grain boundaries.

Zr<sub>3</sub>Y<sub>4</sub>O<sub>12</sub> (D.3 and D.4). This material has a measured density of 97.2% of theoretical. The micrographs show a distribution of submicron pores throughout the sample with most of the pores being within the grains. The grain size varies from less than 5um to greater than 20um.

Zr<sub>3</sub>La<sub>4</sub>O<sub>12</sub> (D.5 and D.6) and Doped Zr<sub>3</sub>La<sub>4</sub>O<sub>12</sub> (D.7 - D.10). With a density 97.5% of theoretical, the undoped material has an even distribution of closed porosity. Most of the pores are larger than 3um. The grains appear equiaxed with a size range of 1 to 10um. The doped materials have densities ranging from 98.0% to 99.1% theoretical and have a microstructure similar to that of the undoped material.

Zr<sub>3</sub>Gd<sub>4</sub>O<sub>12</sub> (D.11 and D.12). This material has a rather low density 94.1% of theoretical, and this is reflected in the micrographs. Closed porosity is evenly distributed with most pores being less than 2um. The pores appear within the grains as well as at the grain boundaries. The grain size is typically less than 10um.

Y<sub>2</sub>O<sub>3</sub> (D.13). The yttria has a measured density 97% of theoretical. The closed porosity appears both within the grains and at the grain boundaries with pores ranging from less than 1um to greater than 5um. Most of the grains are larger than 5um.

CZ101 - Cubic Stabilized Zirconia (D.14). The cubic zirconia material has substantial closed porosity with pore size ranging from less than 1um within the grains to greater than 15um at the grain boundaries.

### X-Ray Diffraction Results

X-ray diffraction traces for all of the materials studied are presented in Appendix E. In all cases, the surfaces of the disc-shaped samples were directly studied. The data were collected on a Scintag diffractometer using Cu K $\alpha$  radiation with a scan speed of 1° 2 $\theta$ /minute and step scan increments of 0.02° 2 $\theta$ . Only the high angle reflections (50-120° 2 $\theta$ ) were used to calculate pseudo-cubic lattice constants. Several of the materials gave patterns including weak reflections in addition to the primary f.c.c. peaks, thus indicating possible formation of ordered compounds. In the case of Zr<sub>3</sub>Sc<sub>4</sub>O<sub>12</sub> the pattern could be indexed to the true rhombohedral (hexagonal) structure. Even when such ordering occurs, giving a different unit cell, the primary reflections can still be indexed based on the f.c.c. structure. In all cases, we are thus able to report a pseudo-cubic lattice parameter. (Most of the diffraction traces also show a weak reflection near 38° 2 $\theta$  arising from the Al sample holder.)

All of the diffraction patterns were analyzed in an attempt to correlate weak "extra" reflections with expected ordered compounds - M<sub>7</sub>O<sub>12</sub> (rhombohedral) or M<sub>4</sub>O<sub>7</sub> (pyrochlore-cubic), as well as the various polymorphic forms of the parent ZrO<sub>2</sub> or M<sub>2</sub>O<sub>3</sub> oxides. As mentioned above, except for the case of Zr<sub>3</sub>Sc<sub>4</sub>O<sub>12</sub>, no match was found. The weak extra reflections could be produced by formation of unknown second phases present in concentrations of a few percent of the primary phase or could result from partial ordering effects on the oxygen sublattice associated with a new "supercell." Within the scope of the present study, we are unable to clarify this issue. Except for Zr<sub>3</sub>Sc<sub>4</sub>O<sub>12</sub>, we therefore regard all of the mixed oxides studied as primarily cubic-solid solutions. Specific comments for each material are as follows.

Zr<sub>3</sub>Sc<sub>4</sub>O<sub>12</sub> (E.1.). This is well crystallized material showing additional reflections characteristic of the M<sub>7</sub>O<sub>12</sub> structure. All peaks could be indexed to the reported hexagonal structure giving  $a_o = 9.395 \pm .001\text{\AA}$ ,  $c_o = 8.725 \pm 0.001\text{\AA}$ . These values are close to the reported values of  $A_o = 9.396$  and  $C_o = 8.720$ . Using pseudo-cubic indexing, the lattice parameter was calculated to be  $a_o = 5.026 \pm 0.002\text{\AA}$ .

Zr<sub>3</sub>Y<sub>4</sub>O<sub>12</sub> (E.2.). Several weak peaks in addition to the primary fluorite-related reflections were observed but could not be indexed. The lack of splitting of the primary f.c.c. reflections expected when ordering gives the rhombohedral M<sub>7</sub>O<sub>12</sub> structure (JCPDS 29-1389), suggests that the material is primarily a disordered solid solution. Indexing as pseudo-cubic gave  $a_0 = 5.222 \pm 0.002\text{\AA}$ .

Zr<sub>3</sub>La<sub>4</sub>O<sub>12</sub> (E.3.) and Doped Zr<sub>3</sub>La<sub>4</sub>O<sub>12</sub> (E.4.). This pattern (as did all of the doped materials based on the La compound) showed an unexpected high degree of (111) orientation such that the intensity ratio for (111)/(200) is about 30/1 compared to a normal ratio of 4/1. Although we did not explore reasons for the preferred orientation, La<sub>2</sub>O<sub>3</sub> is hexagonal, while all of the other trivalent oxides are cubic. Whatever the cause, it seems necessary that the preferred orientation effect must occur early in the fabrication process, probably with formation of the hydroxide, rather than during final sintering. There are weak "extra" reflections which could not be indexed to the M<sub>7</sub>O<sub>12</sub> rhombohedral cell, nor to other possible second phase materials as discussed earlier. The pseudo-cubic lattice constant is  $a_0 = 5.413 \pm 0.001\text{\AA}$ .

The doped Zr<sub>3</sub>La<sub>4</sub>O<sub>12</sub> samples showed very little difference from the parent material. The measured lattice parameters were only slightly changed, even in the case of doping with 5% Sc, where the lattice constant was expected to decrease to 5.394Å, assuming a simple solid solution occurs. The measured value was 5.410Å, only slightly below pure Zr<sub>3</sub>La<sub>4</sub>O<sub>12</sub>, with  $a_0 = 5.413\text{\AA}$ . No evidence for unreacted Sc<sub>2</sub>O<sub>3</sub> could be found; hence, the crystallographic effect of adding Sc<sup>3+</sup> to the lanthanum compound is difficult to understand and outside the scope of the present study.

Zr<sub>3</sub>Gd<sub>4</sub>O<sub>12</sub> (E.5.). This pattern shows no indication of additional reflections other than those characteristic of the fluorite f.c.c. structure, meaning ordering effects, if any, are very short range. The cubic lattice parameter is  $5.2889 \pm 0.0002\text{\AA}$ .

Cubic ZrO<sub>2</sub> (E.6.). The pattern is primarily that of the cubic stabilized structure. Additional weak lines could not be indexed. The cubic lattice parameter is  $a_0 = 5.140 \pm 0.002\text{\AA}$ .

Pseudo-cubic lattice parameters, calculated from reflections in the range  $50-110^\circ 2\theta$ , were given previously, in Table 1, for all of the materials. Figure 4 is a plot of lattice constants for the  $Zr_3M_4O_{12}$  composition plotted as a function of the trivalent cation radius. The  $Zr_3Sc_4O_{12}$  lattice constant is lower than might be expected by a simple linear extrapolation from the rare earth and Y compounds. As discussed later, this regular trend in lattice constants is not matched by a regular trend in diffusivity, although the Sc compound, with the smallest unit cell dimension, does have the lowest oxygen diffusivity.



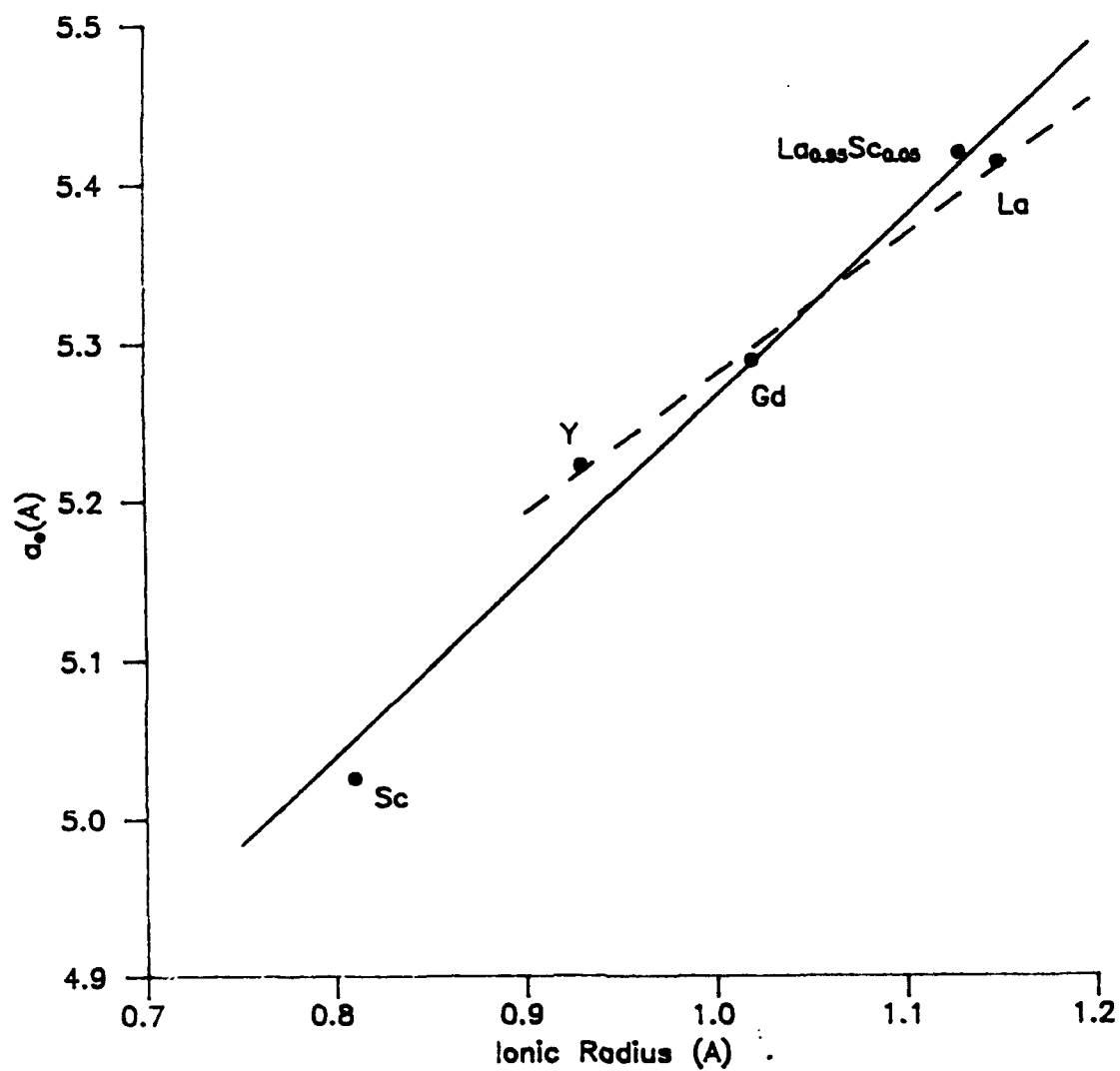


FIGURE 4. Lattice Parameter Versus Cation Radii

## Diffusion Results

Representative experimental data for each of the materials studied are provided in Appendix F as plots of  $^{18}\text{O}$  atom fraction versus time. The solid curves shown were calculated using the program described earlier. The plotting routine utilized ten points connected by straight line approximations, which is sufficient for our curve-matching needs. Figure 5, for  $\text{Zr}_3\text{Sc}_4\text{O}_{12}$  at  $1135^\circ\text{C}$ , shows a representative example of good agreement between the experiment and the "best" calculated curve. Examination of the other data provided in Appendix F demonstrates that the agreement between experiment and theory is very good for  $\text{Y}_2\text{O}_3$ ,  $\text{Zr}_3\text{Sc}_4\text{O}_{12}$ , and  $\text{Zr}_3\text{La}_4\text{O}_{12}$ , but not so good for CZ101 (cubic stabilized zirconia),  $\text{Zr}_3\text{Gd}_4\text{O}_{12}$ , and  $\text{Zr}_3\text{Y}_4\text{O}_{12}$ . In the case of  $\text{Zr}_3\text{Sc}_4\text{O}_{12}$ , the degree of "fit" is better at  $1135^\circ\text{C}$  than at the lower temperatures, where the exchange fraction is very small and experimental errors, for example, exchange with the  $\text{SiO}_2$ , become more important. The three materials showing poor agreement with theory had densities 94-97% of theoretical, compared to 98-99% theoretical density for samples showing good agreement with theory. For the "poor fit" case, a consistent means of selecting the "best"  $D$  value was needed. Using  $\text{Zr}_3\text{Y}_4\text{O}_{12}$  as an example, as shown in Figure F.4, the data are bracketed by theoretical curves ranging from  $D=2\times 10^{-8}$  to  $D=7\times 10^{-8}$ . To treat all such data consistently, we chose the theoretical curve intersecting the experimental data at an  $^{18}\text{O}$  atom fraction of 0.85. For the example shown in Figure F.4, this "best fit" curve gives  $D=4.5\times 10^{-8}$ . Alternative and equally arbitrary methods of considering the "best fit," such as emphasizing the rate of exchange at long times, give different estimated  $D$  values, but the temperature dependence and relative ranking of materials do not change very much.

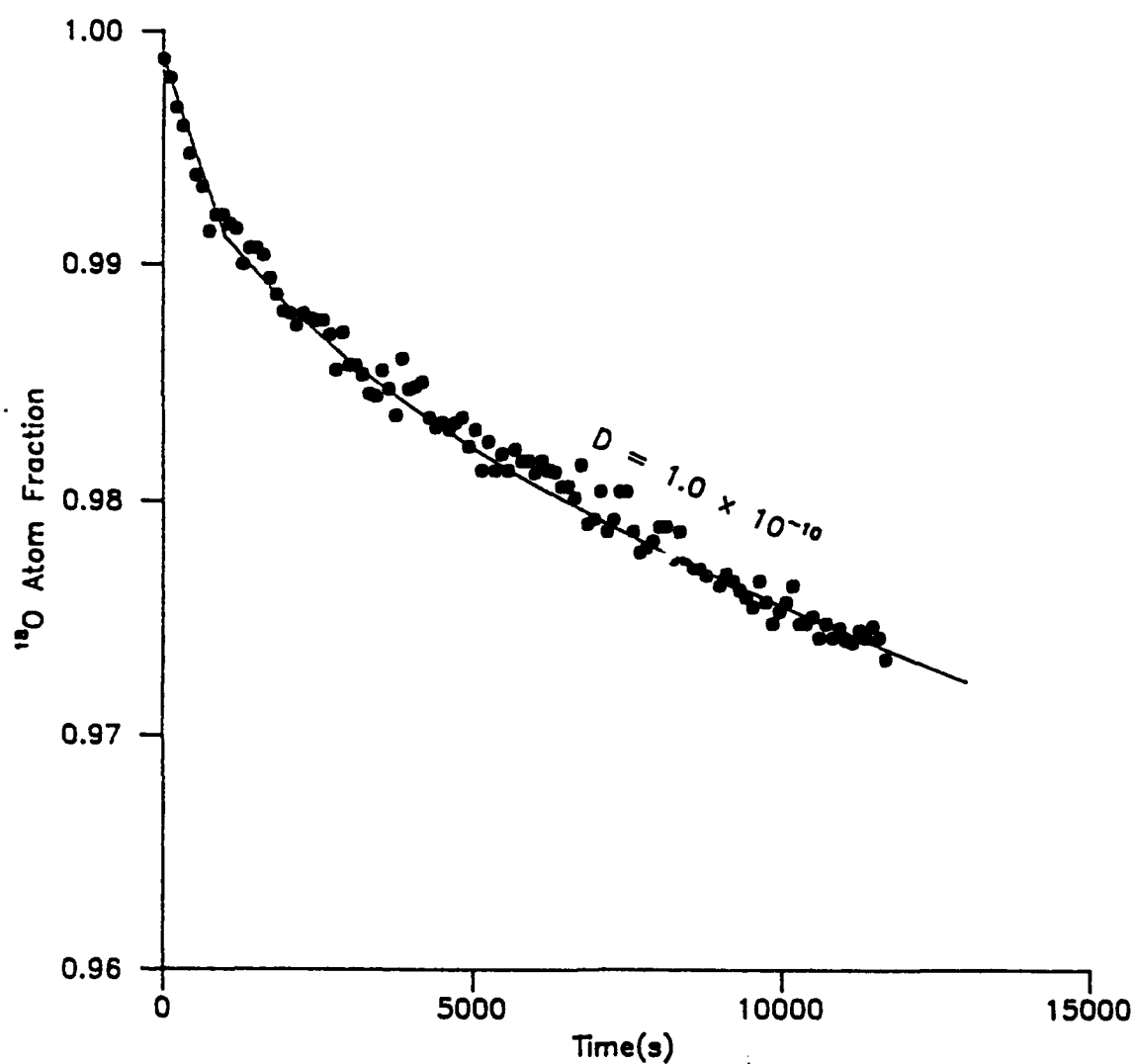


FIGURE 5.  $[^{18}\text{O}]$  Versus Time for  $\text{Zr}_3\text{Sc}_4\text{O}_{12}$  at  $1135^\circ\text{C}$

The final results are best summarized in the form of the well known Arrhenius plot, where  $\log_{10} D$  vs  $1/T$  gives straight lines as provided in Figure 6. The materials differ in diffusivity by two to three orders of magnitude, with  $D$  ranging from  $10^{-7}$  to  $10^{-10}$   $\text{cm}^2/\text{s}$  at  $1135^\circ\text{C}$ , as shown in Table 2. Table 3 summarizes the results in terms of the straight line constants corresponding to the equation -

$$\log D = \log D_0 - E_a/RT$$

There were no discernible trends in  $D_0$  or  $E_a$  with regard to cubic lattice parameters.  $\text{Zr}_3\text{Sc}_4\text{O}_{12}$  which had the smallest lattice parameter, did have the lowest diffusivity and the highest activation energy. It is also the only mixed oxide studied which was determined to be fully ordered. Insofar as these diffusion constants are based on a very small data set of only 3 points per line, no detailed examination is warranted. Interpretation is further complicated by the microstructural differences between the different materials and evidence for non-Fickian diffusion, especially for samples with density  $\leq 97\%$  of theoretical. If porosity provides a fast path for diffusion, the diffusion coefficients measured for some of the materials in this study will be high compared to true bulk diffusion values.

The diffusivities of the doped  $\text{Zr}_3\text{La}_4\text{O}_{12}$  materials were measured at  $1135^\circ\text{C}$ . The agreement between the theoretical model and the experimental gas concentration-time curve was good for all these samples, as shown in Figures F.6 through F.9. As shown in Table 2, the diffusion coefficients for the materials doped with both scandium and tantalum were slightly lower than that of the undoped material. The measured diffusion coefficient for the  $\text{Zr}_3\text{La}_4\text{O}_{12}$  doped with 5% scandium was higher than the undoped material and higher than the materials doped with both scandium and tantalum. As mentioned previously, the lattice parameter of this material was also higher than the other doped materials and approached that of the undoped material.

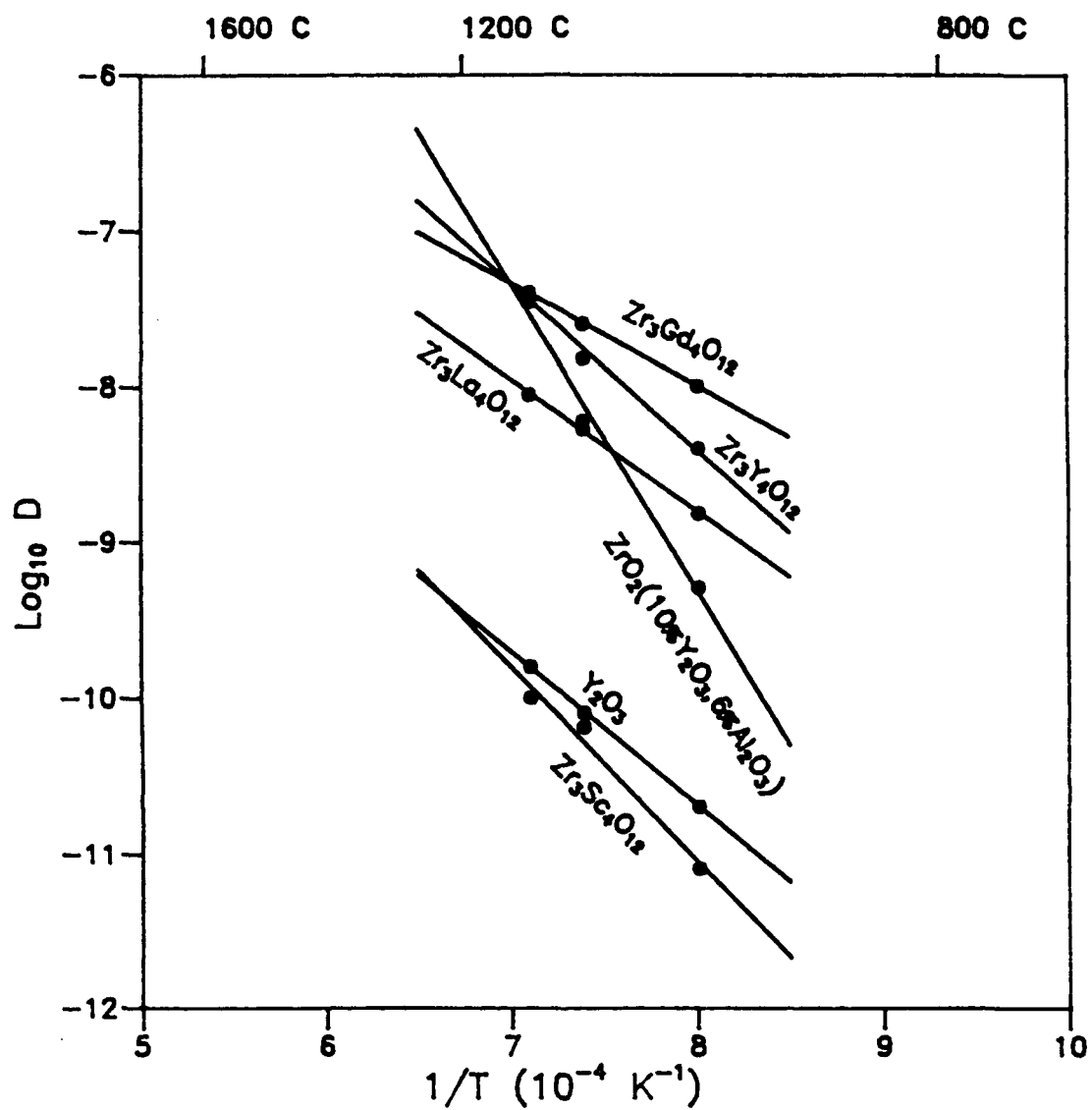


FIGURE 6. Temperature Dependence of Oxygen Diffusivity

TABLE 2. Measured Diffusion Coefficients

Material	Temperature (C)	D(cm <sup>2</sup> /sec)
Zr <sub>3</sub> Sc <sub>4</sub> O <sub>12</sub>	975	8.0 x 10 <sup>-12</sup>
	1080	6.5 x 10 <sup>-11</sup>
	1135	1.0 x 10 <sup>-10</sup>
Zr <sub>3</sub> Y <sub>4</sub> O <sub>12</sub>	975	4.0 x 10 <sup>-9</sup>
	1080	1.5 x 10 <sup>-8</sup>
	1135	4.0 x 10 <sup>-8</sup>
Zr <sub>3</sub> Gd <sub>4</sub> O <sub>12</sub>	975	1.0 x 10 <sup>-8</sup>
	1080	2.5 x 10 <sup>-8</sup>
	1135	4.0 x 10 <sup>-8</sup>
Zr <sub>3</sub> La <sub>4</sub> O <sub>12</sub>	975	1.5 x 10 <sup>-9</sup>
	1080	5.4 x 10 <sup>-9</sup>
	1135	9.0 x 10 <sup>-9</sup>
Zr <sub>2.98</sub> Sc <sub>0.01</sub> Ta <sub>0.01</sub> La <sub>4</sub> O <sub>12</sub>	1135	6.0 x 10 <sup>-9</sup>
Zr <sub>2.9</sub> Sc <sub>0.05</sub> Ta <sub>0.05</sub> La <sub>4</sub> O <sub>12</sub>	1135	5.5 x 10 <sup>-9</sup>
Zr <sub>2.7</sub> Sc <sub>0.15</sub> Ta <sub>0.15</sub> La <sub>4</sub> O <sub>12</sub>	1135	4.0 x 10 <sup>-9</sup>
Zr <sub>3</sub> La <sub>3.8</sub> Sc <sub>0.2</sub> O <sub>12</sub>	1135	1.5 x 10 <sup>-8</sup>
CZ101 (Cubic Stabilized Zirconia)	975	5.0 x 10 <sup>-10</sup>
	1080	6.0 x 10 <sup>-9</sup>
	1135	3.5 x 10 <sup>-8</sup>
Y <sub>2</sub> O <sub>3</sub>	975	2.0 x 10 <sup>-11</sup>
	1080	6.0 x 10 <sup>-11</sup>
	1135	1.6 x 10 <sup>-10</sup>

**TABLE 3. Activation Energies and  $D_0$  for Undoped Materials**

<b>Material</b>	<b><math>D_0(\text{cm}^2/\text{sec})</math></b>	<b><math>E_a(\text{kJ/mol})</math></b>	<b><math>a_0(\text{\AA})</math></b>
$\text{Zr}_3\text{Sc}_4\text{O}_{12}$	$8.3 \times 10^{-2}$	239	5.026
$\text{Zr}_3\text{Y}_4\text{O}_{12}$	1.5	205	5.222
$\text{Zr}_3\text{Gd}_4\text{O}_{12}$	$1.9 \times 10^{-3}$	126	5.289
$\text{Zr}_3\text{La}_4\text{O}_{12}$	$1.2 \times 10^{-2}$	165	5.413
CZ101	$3.5 \times 10^6$	379	5.140
$\text{Y}_2\text{O}_3$	$9.6 \times 10^{-4}$	184	-----

### RELATED WORK

In Figure 7, the results of this study, shown as dashed lines, are compared to the previously published diffusion data for several related oxides, shown as solid lines. The diffusion behavior observed in the  $\text{Zr}_3\text{M}_4\text{O}_{12}$  materials is well within the range observed in several fluorite related oxides, including stoichiometric  $\text{UO}_2$  (Murch, 1983),  $\text{ThO}_2$  (Ando, 1976),  $\text{Pr}_7\text{O}_{12-\delta}$  (Lau, 1976), and  $70\text{ZrO}_2-30\text{Y}_2\text{O}_3$  (Oishi, 1985). Previous studies of single crystal  $\text{Y}_2\text{O}_3$  (Ando, 1985) gave diffusion coefficients approximately two orders of magnitude smaller than those observed for the polycrystalline  $\text{Y}_2\text{O}_3$  in this study.

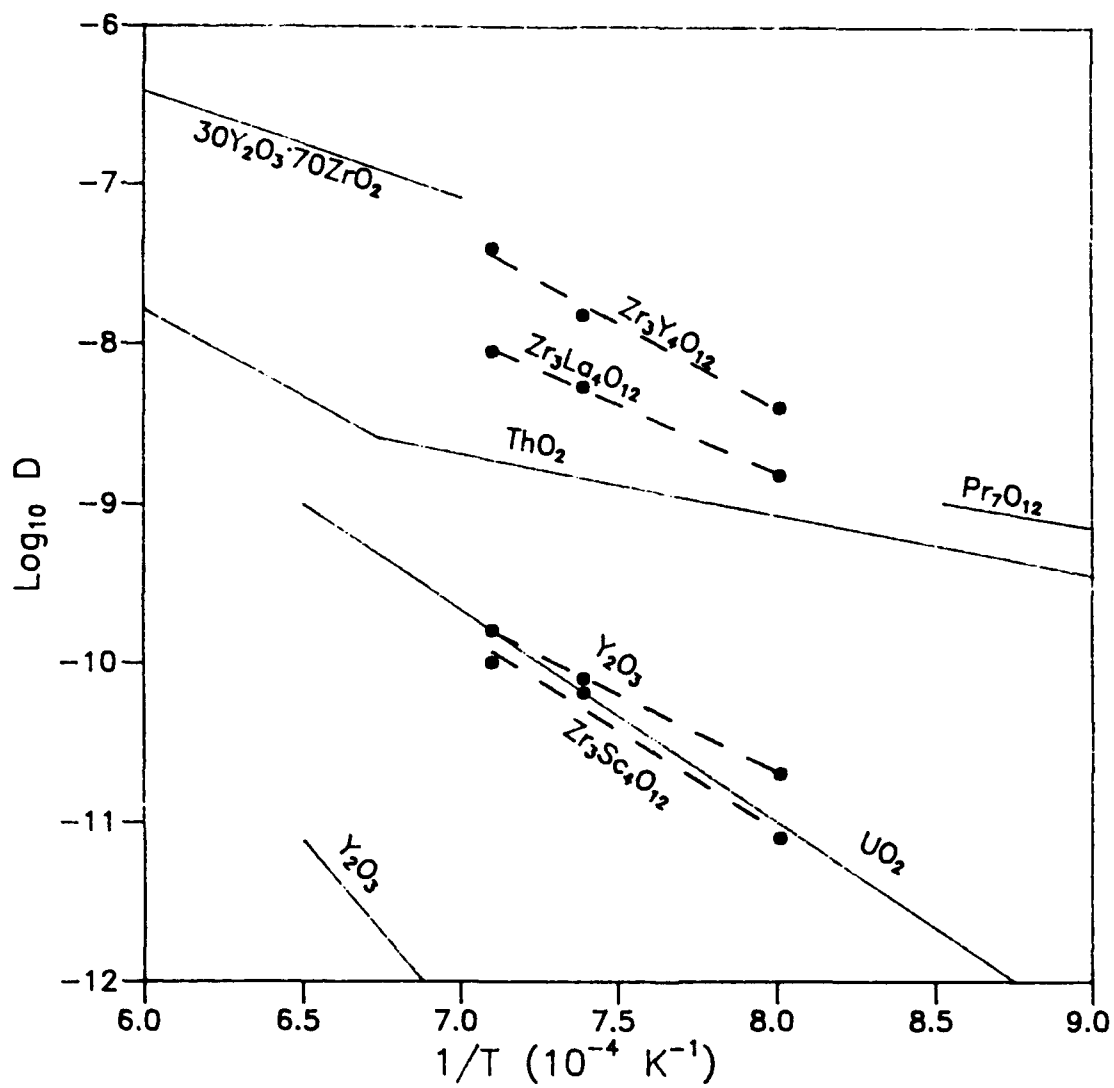


FIGURE 7. Comparison of Oxygen Diffusivity of Related Oxides  
(--- this study, — literature)



## CONCLUSIONS

For the mixed oxide samples examined, the diffusivity spanned three orders of magnitude with  $D$  ranging from  $10^{-7}$  to  $10^{-10}$  at  $1135^{\circ}\text{C}$ . These results are comparable to the diffusion behavior observed in other fluorite-related oxides.

$\text{Zr}_3\text{Sc}_4\text{O}_{12}$ , which had the smallest unit cell dimension and trivalent cation radius, had the lowest diffusivity and highest activation energy of the mixed oxides studied. Furthermore, this is the only mixed oxide studied which was fully ordered. No further relationship was found between the ionic radius of the trivalent cation and oxygen diffusivity. However, non-Fickian diffusion was observed for two of the mixed oxides; their apparent high diffusion coefficients may be related to their higher porosity.

Doping  $\text{Zr}_3\text{La}_4\text{O}_{12}$  with  $\text{Sc}^{3+}$  or with  $\text{Sc}^{3+}/\text{Ta}^{5+}$  had only a small effect on the oxygen diffusivity.

The preparation of dense pore-free samples proved difficult for the  $\text{Zr}_3\text{M}_4\text{O}_{12}$  systems. A suitable fabrication process was developed giving densities as high as 99% of theoretical values but was not fully optimized. By optimizing dispersant concentration and firing schedules, it is likely that ceramics near 100% density can be prepared for these compositions and related mixed oxides.

Although the melting points for  $\text{Zr}_3\text{M}_4\text{O}_{12}$  oxides are higher than for the pure rare earth oxides or yttria, there is no oxygen diffusivity advantage over pure  $\text{Y}_2\text{O}_3$ , based on this study.

## REFERENCES

1. Ando, K., Y. Oishi, and Y. Hidaka. 1976. "Self-diffusion of Oxygen in Single Crystal Thorium Oxide." J. Chem. Phys. (65):2751-2755.
2. Ando, K. and Y. Oishi. 1985. "Oxygen Self-diffusion in  $Y_2O_3$  and  $Y_2O_3$ - $ZrO_2$  Solid Solution." In NATO ASI Series, Ser.B., Vol.129, Transport in Nonstoichiometric Compounds, ed. G. Simkovich and V.S. Stubican, 203-215.
3. Lau, K.H., D.L. Fox, S.H. Lin, and L. Eyring. 1976. "Oxygen Transport in Polycrystals and Single Crystals of  $Pr_7O_{12\pm\delta}$ ." High Temp. Sci. (8):129-139.
4. Murch, G.E. 1983. "Oxygen Diffusion in Uranium Oxide - An Overview." Diffusion and Defect Data (32):9-19
5. Oishi, Y. and K. Ando. 1985. "Oxygen Self-diffusion in Cubic  $ZrO_2$  Solid Solutions." In NATO ASI Series, Ser.B., Vol. 129, Transport in Nonstoichiometric Compounds, ed. G. Simkovich and V.S. Stubican, 189-202.

## APPENDIX A PRELIMINARY PROCESSING

A significant effort was required to develop procedures which eventually produced homogeneous pellets with densities near 98% of theoretical density. This appendix summarizes results of the preliminary effort, including: 1) coprecipitation and pressureless sintering, 2) coprecipitation and hot-pressing, and 3) coprecipitation with dispersant and pressureless sintering.

### Coprecipitation and Pressureless Sintering

Nitrate salts were dissolved in hot de-ionized water using teflon beakers and hot-plate stirring. In most cases, a very small amount of insoluble material was observed, probably pure oxide. All of the starting materials were 99.9% pure, or better.

In some experiments, ammonium hydroxide solution was added to the nitrate solution, resulting in a gelatinous material containing the metal hydroxides, ammonium nitrate, excess ammonia, and water. In other experiments, the mixed nitrate solution was added to the ammonium hydroxide, thus maintaining a high pH and insuring a uniform coprecipitation. Both methods yielded a mixture that separated into an aqueous phase and a gelatinous phase within an hour after precipitation. The mixtures were either dried overnight in air at 110°C or centrifuged, washed with ammonium hydroxide solution, and then dried in air at 110°C. The dried hydroxide produced a virtually featureless X-ray diffraction pattern suggesting a noncrystalline powder or one composed of extremely small crystallites, which was the desired result.

The hydroxide was calcined between 350°C and 700°C in air to convert it to oxide and to decompose any ammonium nitrate and excess ammonium hydroxide. The calcined powder was crushed with a mortar and pestle, pressed into pellets 1/2 inch diameter by 1/8 inch thick, and fired to 1680°C for 6 hours using yttria-stabilized zirconia crucibles.

Most of the work was performed on the Zr/Y system. As shown in Table A.1, the densities of the sintered pellets were generally low and ranged from 3.49 to

4.02 g/cm<sup>3</sup> (<75% theoretical density). Limited work with the Zr/Gd system also gave pellets with low densities less than 86% of theoretical. Sintered pellets of the  $Zr_3La_4O_{12}$  crumbled, and their densities were not measured.

**TABLE A.1. Processing Conditions**

Composition	Precipitation	Calcine Temp	Pressing Pressure (psi)	Density (g/cm <sup>3</sup> )	% Open Porosity
Y/Zr	NH <sub>4</sub> OH into nitrates dry 110C in air	700C	34K	3.54	25.6
Y/Zr	NH <sub>4</sub> OH into nitrates dry 110C in air	700C	45K	3.63	22.2
Y/Zr*	NH <sub>4</sub> OH into nitrates dry 110C in air	700C	34K	3.49	22.6
Y/Zr	Nitrates into NH <sub>4</sub> OH dry 110C in air	600C	45K	3.80	21.7
Y/Zr	Nitrates into NH <sub>4</sub> OH dry 110C in air	500C	45K	3.87	19.9
Y/Zr	Nitrates into NH <sub>4</sub> OH dry 110C in air	400C	56K	3.97	15.7
Y/Zr	Nitrates into NH <sub>4</sub> OH dry 110C in air	400C	45K	3.97	16.1
Y/Zr	Nitrates into NH <sub>4</sub> OH dry 110C in air	350C	45K	4.02	14.1
Y/Zr	Separate nitrates into NH <sub>4</sub> OH, mix gels, dry 110C in air	500C	45K	3.48	26.1
Y/Zr	NH <sub>4</sub> OH into nitrates, centrifuge, dry 110C in air	500C	45K	3.87	21.0
Gd/Zr	NH <sub>4</sub> OH into nitrates, dry 110C in air	700C	34K	4.40	22.8
Gd/Zr	Nitrates into NH <sub>4</sub> OH dry 110C in air	350C	45K	5.07	14.8
La/Zr	NH <sub>4</sub> OH into nitrates dry 110C in air	700C	34K	pellets crumbled	
La/Zr	Nitrates into NH <sub>4</sub> OH dry 110C in air	350C	45K	pellets crumbled	

\*sintering time of 24 hours, 1680°C; all others 6 hours, 1680°C

A number of organic additives were examined to improve sintering in the Zr/Y system. Powders calcined at 350°C-400°C were dispersed in the additive systems using a sonicator, Heat Systems Ultrasonics Model W-375. The slurries were dried at 110°C in air. Pellets were pressed at 45,000 psi and fired at 1680°C for 6 hours. As shown in Table A.2, there was no notable increase in the densities of pellets prepared with additives, and in the case of the paraffin/fish oil/toluene system, the density decreased significantly.

**TABLE A.2. Density of  $Zr_3Y_4O_{12}$  Prepared with Additives**

Additive	Density	%Open Porosity
Carbowax 8000/MeOH	3.41	31.2
Carbowax 3500/MeOH	4.08	19.9
Carbowax 3500/MeOH/ Solsperse 3000	3.75	28.2
Paraffin/fish oil/ toluene	2.67	48.3

Ideally, particles should grow uniformly and equiaxially during sintering. Rapid growth of highly reactive sites on the powders at lower temperatures can cause bridging and inhibit further densification. To reduce this effect, samples were pressed and prefired to temperatures lower than the sintering temperature, recrushed using a mortar and pestle, repressed, and fired to the final sintering temperature of 1680°C. Because the recrushing of the pellets is difficult, loose powder was also prefired. Figure A.1 illustrates the effect of the prefiring temperature on the density of the pellet after final sintering. The densities increased with prefiring temperature, and the densities of materials prefired as a pellet were slightly better than those prefired as powder. However, at a prefiring temperature of 1680°C, the final pellet density was only 4.36 g/cm<sup>3</sup> which is about 81% of theoretical density.

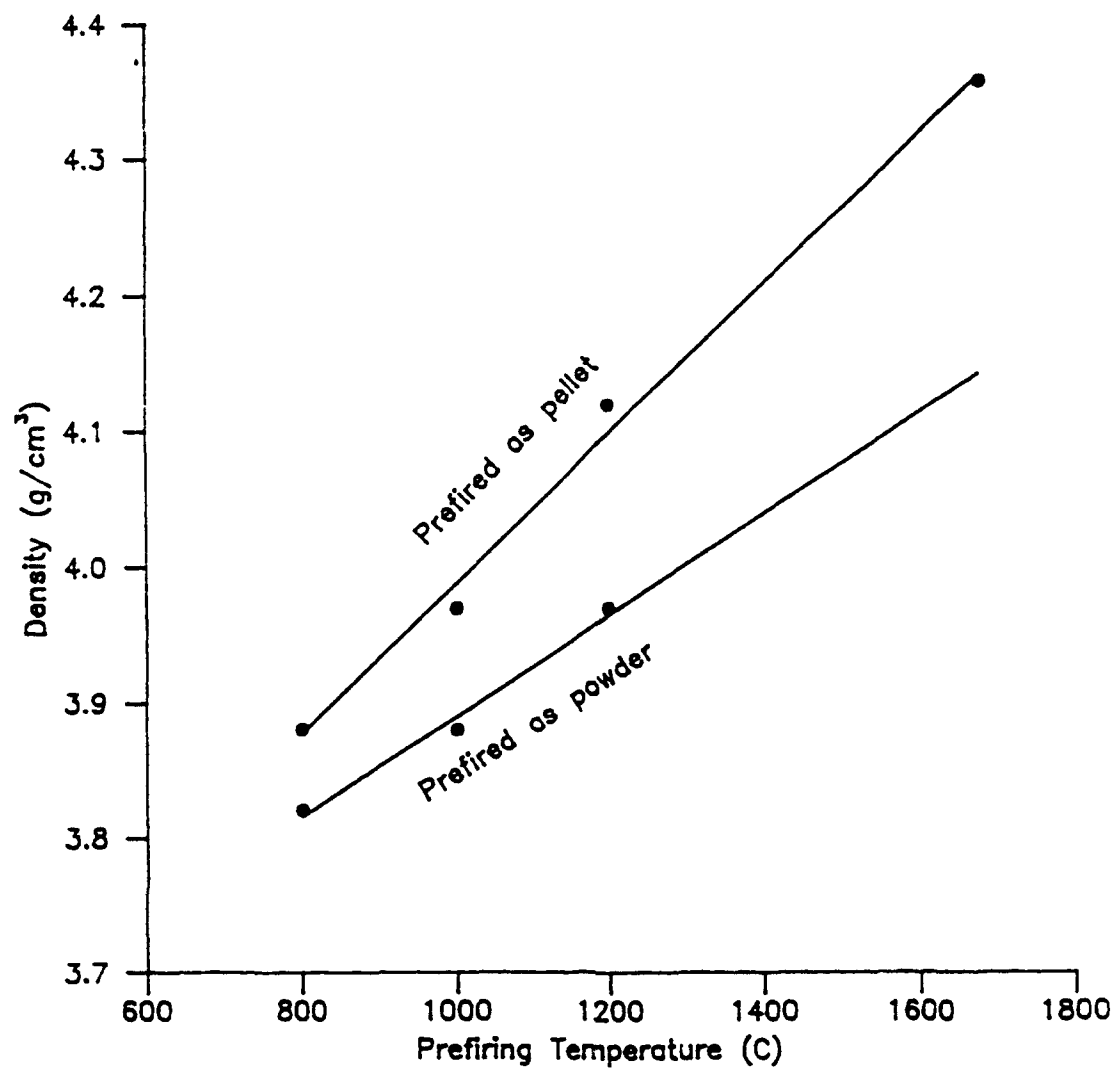


**FIGURE A.1. Effect of Prefiring Temperature on Fired Pellet Density**

To reach high density using very high temperature as the driving force, pellets of  $Zr_3Y_4O_{12}$  were fired to 2100°C for 6 hours in a helium atmosphere, using a graphite resistance furnace. While the density increased, the pellets were brown, indicating some reduction. The pellets were reoxidized by heating in air to 1680°C with no notable change in density or porosity. A density of 4.79 g/cm<sup>3</sup>, or about 88% theoretical, was achieved with this method, which was still unacceptable for the intended diffusion study. Microstructural examination of the calcined powders and pellets suggested so-called "hard-agglomerates" were responsible for the low densities. It was decided to attempt hot pressing the ceramics.

#### Coprecipitation and Hot Pressing

Powders of  $Zr_3Y_4O_{12}$ ,  $Zr_3Gd_4O_{12}$ , and  $Zr_3La_4O_{12}$  were prepared for hot pressing by adding the mixed nitrate solutions to excess ammonium hydroxide. The resultant solution was dried at 110°C overnight. To facilitate complete removal of the ammonium nitrate and excess ammonium hydroxide, the powders were calcined at 600°C under vacuum.

The samples were hot pressed in graphite dies at 1500°C for one hour with a maximum load condition of 14,000 psi applied at temperature. As expected, the hot-pressed ceramics (large pellets 1 inch diameter by 1/2 inch thick) were black as a result of partial reduction, but gave densities very near to 100% theoretical. Attempts were made to reoxidize the materials by very slow air firing as described below. Measured densities are summarized in Table A.3.

**TABLE A.3. Densities of Hot-Pressed Material**

Composition	As Pressed	Density(g/cm <sup>3</sup> )	
		After Oxidation	After Annealing
Zr/Y	5.34	5.27	5.06
Zr/Gd	6.97	6.52	----
Zr/La	6.06	----	----



A thin slice of the Zr/Y ceramic was cut from the hot-pressed slug and heated to 1050°C over a period of 6 days, held at temperature for 2 days, and cooled to room temperature over a period of 4 days, resulting in a dense cream-colored ceramic. After this oxidation, the sample was annealed by heating at 1°C/min to 1680°C, holding for 10 hours, and cooling to room temperature at 1°C/min. The density decreased as a result of the oxidation at 1050°C, and even more with annealing at 1680°C, to 5.06 g/cm<sup>3</sup>, which is only 92% of theoretical.

Scanning electron microscopy was used to examine changes in microstructure with heat treatment. The fracture surface of the Zr/Y ceramic after hot pressing is shown in the scanning electron micrograph of Figure A.2. The grain size ranges from 3 to 10 μm with some porosity at the grain boundaries.

After heating to 1050°C the grains appear to be equiaxed with most grains being less than 5 μm, as shown in Figure A.3.

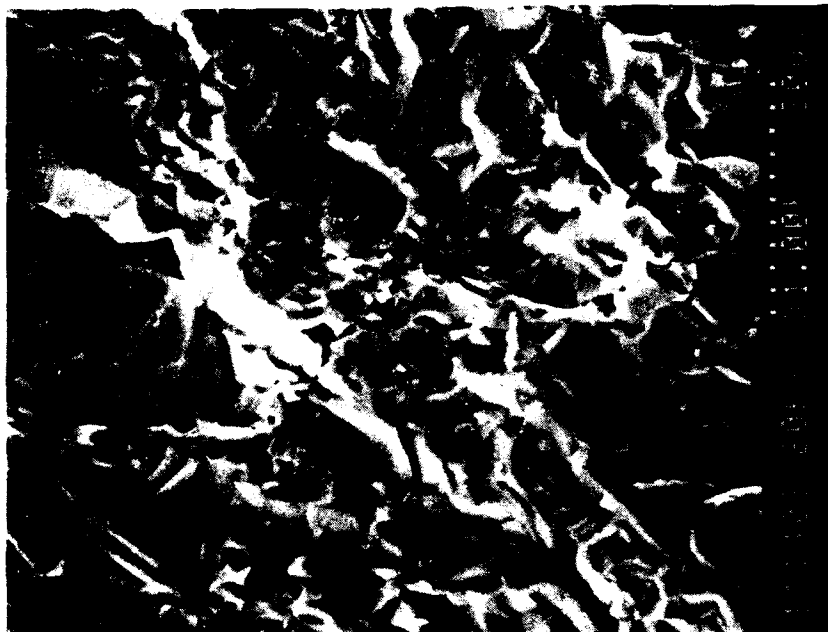


FIGURE A.2. Micrograph of "As Hot-Pressed"  $\text{Zr}_3\text{Y}_4\text{O}_{12}$

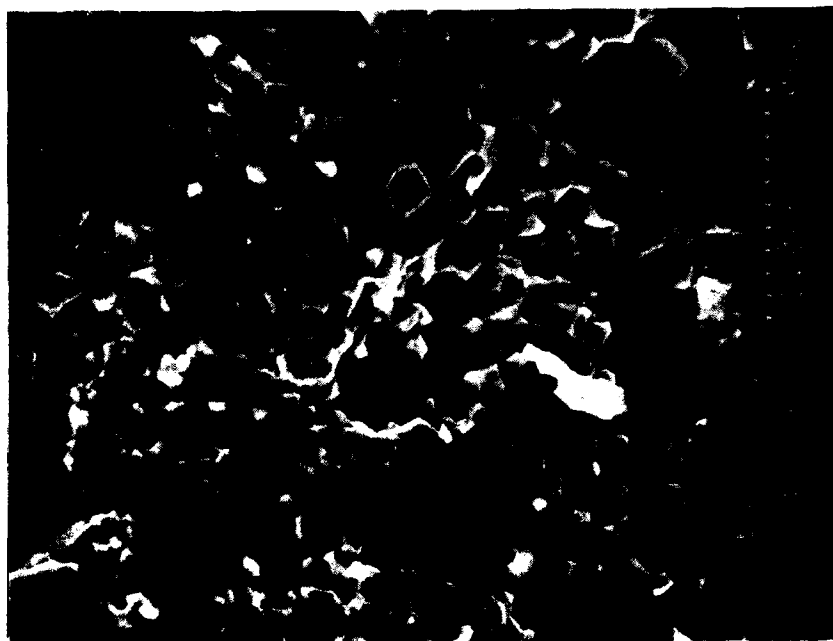


FIGURE A.3. Micrograph of  $\text{Zr}_3\text{Y}_4\text{O}_{12}$  After Oxidation

After annealing to 1680°C, there is extensive porosity at the grain boundaries as illustrated in the scanning electron micrograph of Figure A.4.



FIGURE A.4. Micrograph of  $\text{Zr}_3\text{Y}_4\text{O}_{12}$  After Anneal

A portion of  $\text{Zr}_3\text{Gd}_4\text{O}_{12}$  was heated slowly (1°C/min) to 1600°C, held at temperature for 40 hours, and cooled at 1°C/min to room temperature. The resulting material was pale yellow and very brittle. No density measurements could be taken. In another attempt to reoxidize this material, a sample was heated at 3°C/min to 200°C then to 1680°C at 0.1°C/min, and finally cooled to room temperature at 3°C/min. Scanning electron microscopy of the annealed sample revealed grain boundary decoration similar to the  $\text{Zr}_3\text{Y}_4\text{O}_{12}$ .

Upon storage in air, the hot pressed  $\text{Zr}_3\text{La}_4\text{O}_{12}$  decomposed to a grey powder, and no further heat treatment was examined.

Because of the "best case" porous microstructures and relatively low final densities (93% theoretical), the hot-pressing route to sample fabrication was abandoned.

### Coprecipitation with Dispersant and Pressureless Sintering

Formation of the hydroxide gel from the precipitation of the nitrates by ammonium hydroxide led to a highly agglomerated powder as described in the previous sections. Darvan C, an ammonium polymethacrylate dispersant manufactured by R.T. Vanderbilt, Inc., and Lignosol TSD, an ammonium lignosulfonate dispersant produced by Daishowa Chemical, Inc., were examined as a means of controlling the hydroxide precipitation and subsequent drying. Instead of using the dispersant during a ball milling procedure as in traditional ceramics processing, the additives were used during the precipitation of the hydroxide. Solutions of the nitrate salts were added with rapid mixing to an ammonium hydroxide solution containing the dispersing agent, which was added as a weight percentage of the theoretical yield of  $Zr_3M_4O_{12}$ . The resulting mixtures were more stable colloidal suspensions than previously obtained, with no settling observed over a few-hour period. The suspensions were dried in air at 100°C or centrifuged, washed with ammonium hydroxide, and then dried in air at 100°C, with equivalent results. The dried material was calcined at 650°C for one hour.

Sintered pellets pressed at 45,000 psi from these "as calcined"  $Zr_3Y_4O_{12}$  powders had improved densities over sintered pellets prepared with no dispersant. As can be seen on Table A.4, the densities for the material made with dispersant ranged from 3.47 g/cm<sup>3</sup> to 4.86 g/cm<sup>3</sup>, compared to a density range of 3.49 g/cm<sup>3</sup> to 4.02 g/cm<sup>3</sup> for materials prepared without dispersant. Limited work with  $Zr_3Gd_4O_{12}$  produced pellets with about 75% theoretical density. Pellets of  $Zr_3La_4O_{12}$  disintegrated into a white powder with prolonged exposure to air, as did the material prepared with no dispersants.

**TABLE A.4. Densities of Materials Prepared with Dispersant**

Composition	Additive (wt%)	Density (g/cm <sup>3</sup> )	Open Porosity (%)
Zr/Y	0.5%L	3.47	25.1
Zr/Y	0.5%D	3.65	22.9
Zr/Y	2.5%L	3.61	21.6
Zr/Y	5.0%L	4.20	13.6
Zr/Y	5.0%D	4.17	21.1
Zr/Y	10 %L	4.68	6.1
Zr/Y	10 %D	4.10	20.2
Gd/Y	2.5%L	5.24	21.0

L=Lignosol TDS(ammonium lignosulfonate)  
D=Darvan C(polymethylmethacrylate)

Major improvements were achieved with additional post-calcine processing, as shown in Table A.5. In general, prefiring of the powder to 1600°C followed by ball milling in toluene and zirconia media led to marked increases in sintered pellet density for all three compositions. For example, the density of sintered pellets of  $Zr_3Gd_4O_{12}$  prepared with 2.5% Lignosol TSD increased from 5.24 g/cm<sup>3</sup> to 6.73 g/cm<sup>3</sup> (>96% theoretical density) with this post-calcine process. Additionally, sintered pellets of  $Zr_3La_4O_{12}$  made from prefired powder did not disintegrate with prolonged contact to air and were olive-green in color compared to white pellets from materials with no post-calcine processing.

**TABLE A.5. Densities of Materials with Post-Calcine Processing**

Composition	Additive	Post-Calcine Process	Open Density (g/cm <sup>3</sup> )	Porosity (%)
Zr/Y	0.5%L	900°C prefire + 24 hr ball mill	4.73	3.0
Zr/Y	0.5%D	900°C prefire + 24 hr ball mill	4.58	4.4
Zr/Y	2.5%L	900°C prefire + 24 hr ball mill	5.22	2.7
Zr/Y	5.0%L	900°C prefire + 24 hr ball mill	4.77	1.5
Zr/Y	5.0%D	1600°C prefire + 24 hr ball mill	5.08	2.9
Zr/Y	10% L	1600°C prefire + 24 hr ball mill	5.39	0.2
Zr/Y	10% D	1600°C prefire + 24 hr ball mill	5.14	10.0
Zr/Gd	2.5%L	1600°C prefire + 24 hr ball mill	6.73	0.3
Zr/La	2.5%L	1600°C prefire + 24 hr ball mill	6.75	1.6

L = Lignosol TDS (ammonium lignosulfonate)

D = Darvan C (ammonium polymethacrylate)

The best densities were achieved with material prepared with 2.5% and 10% ammonium lignosulfonate additive. However thermogravimetric analysis of this material indicated a residual ash of nearly 2 wt % remained after heating to 900°C. The components of the ash were identified using energy dispersive X-ray spectroscopy and included sodium, magnesium, silicon, calcium, potassium, iron, and sulfur. Darvan C left no residual ash and therefore was used in the preparation of the materials for the diffusion study.

## APPENDIX B THERMOGRAMS OF STARTING MATERIALS

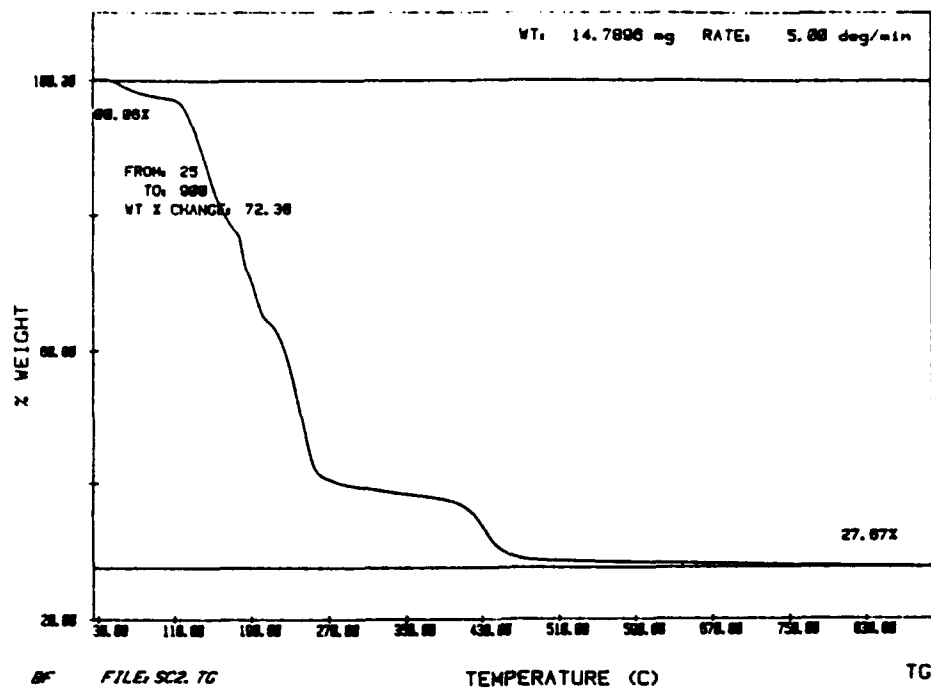


FIGURE B.1. Thermogram for Scandium Nitrate Tetrahydrate

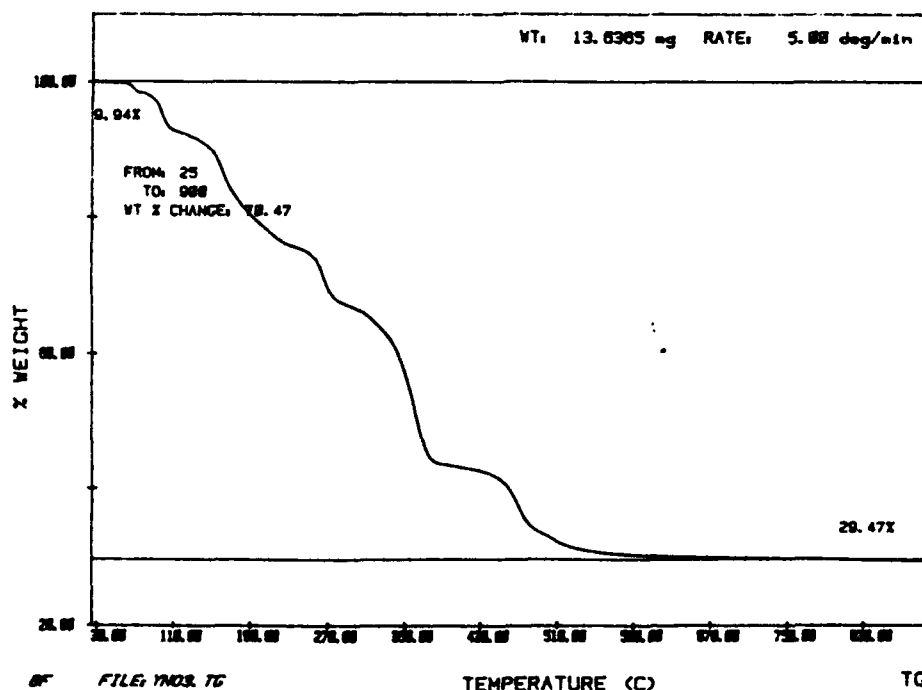


FIGURE B.2. Thermogram for Yttrium Nitrate Hexahydrate

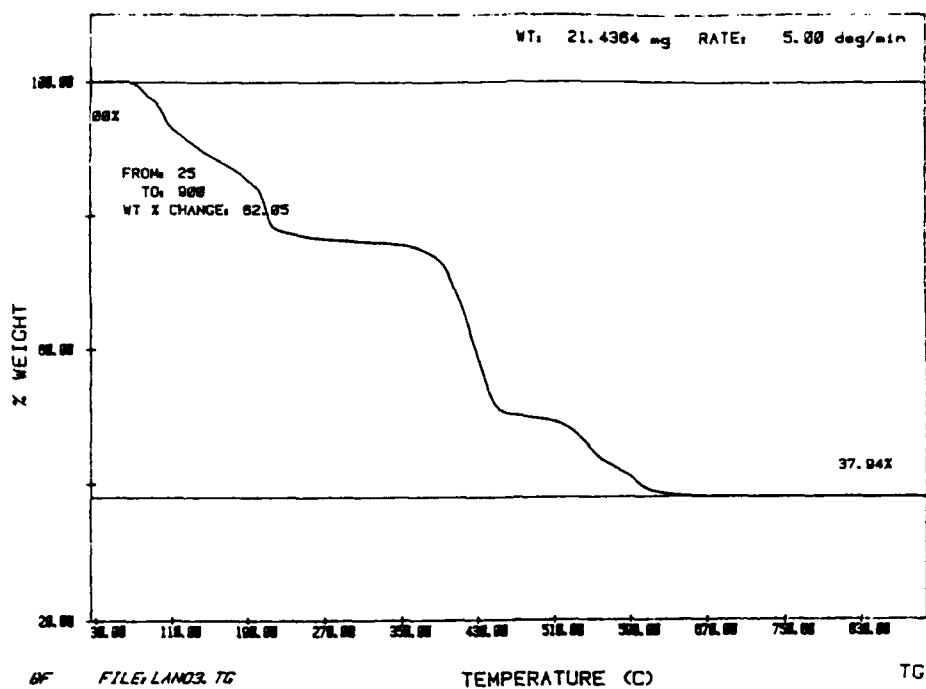


FIGURE B.3. Thermogram for Lanthanum Nitrate Hexaahydrate

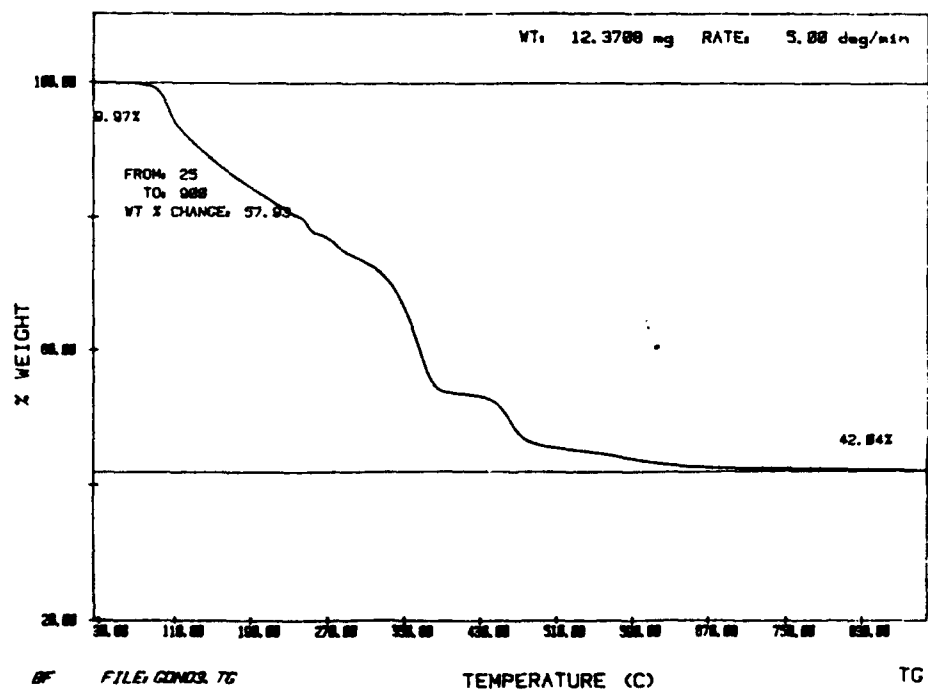


FIGURE B.4. Thermogram for Gadolinium Nitrate Pentahydrate



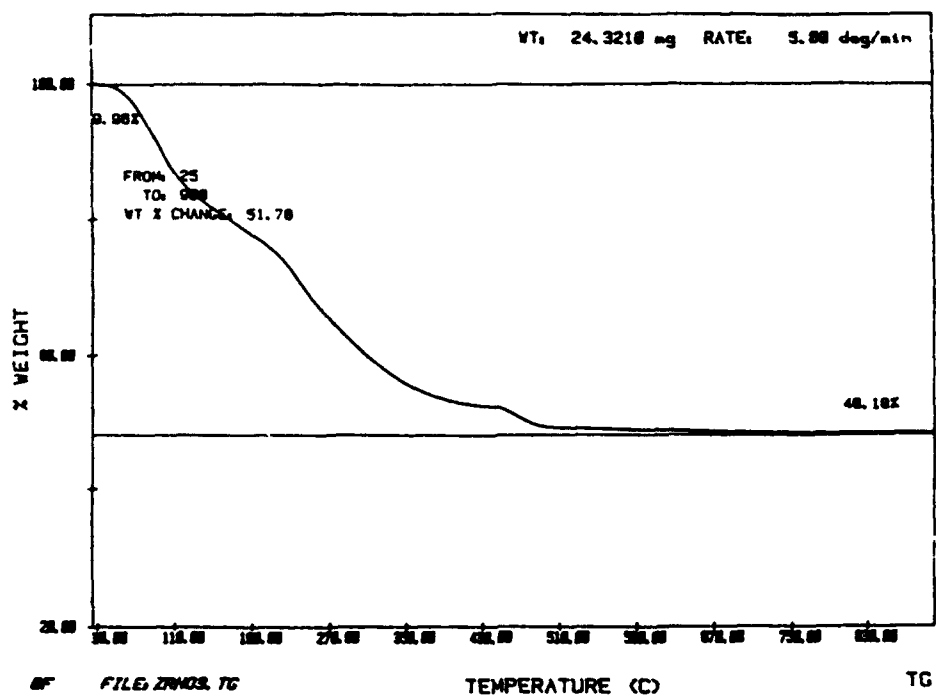


FIGURE B.5. Thermogram for Zirconyl Nitrate

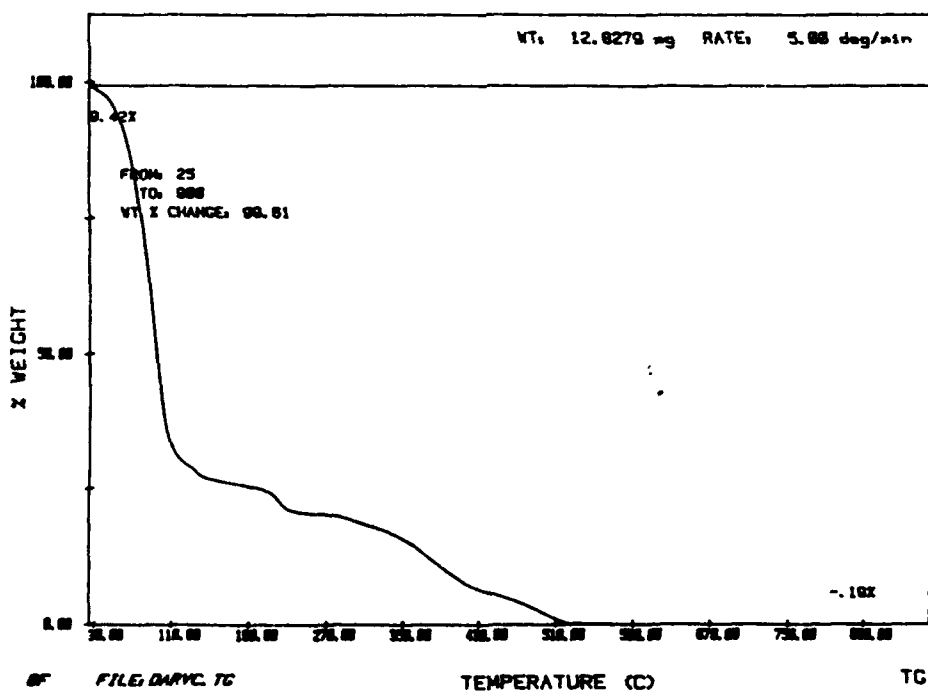


FIGURE B.6. Thermogram for Darvan C, an Ammonium Polymethacrylate Additive

## APPENDIX C    COMPUTER PROGRAM FOR CALCULATING THEORETICAL CURVES

```
PROGRAM DIFF
OPEN(8,FILE='THEODAT')
REWIND 8
DIMENSION ALPHA(1005)
REAL L,LAM
1  FORMAT(1A10)
25  FORMAT (A8,E10.2)
26  FORMAT(I8,2X,F10.8)
CHARACTER CHOICE*10,TAG*8
TAG=' D = '
110 PRINT*,'INPUT THE RATIO OF THE TOTAL NUMBER OF OXYGEN'
PRINT*,'ATOMS IN THE GAS TO THE TOTAL NUMBER OF OXYGEN ATOMS'
PRINT*,'IN THE SOLID.'
READ*,LAM
PRINT*,'NOW CALCULATING THE FIRST 1000 ROOTS'
PRINT*,'OF THE AUXILLIARY EQUATION'
CALL AUXROOTS(LAM,ALPHA)
310 PRINT*,'INPUT SLAB THICKNESS IN CM'
READ*,L
PRINT*,'INPUT INITIAL O-18 ATOM FRACTION IN GAS'
READ*,P2
PRINT*,'INPUT INITIAL O-18 ATOM FRACTION IN SYSTEM'
READ*,P0
120 PRINT*,'ENTER THE DIFFUSION CONSTANT'
READ*,D
150 PRINT*,' '
260 PRINT*,'LE MENU'
PRINT*,'A.      CHANGE PARAMETERS EXCLUDING LAMBDA'
PRINT*,'B.      CHANGE D'
PRINT*,'C.      CALCULATE GAS O-18 PARTIAL PRESSURE VS TIME'
PRINT*,'D.      EXIT PROGRAM'
PRINT*,'INPUT CHOICE'
READ(5,1) CHOICE
IF(CHOICE.EQ.'A')THEN
    GOTO 310
ENDIF
IF(CHOICE.EQ.'B')THEN
    GOTO 120
ENDIF
IF(CHOICE.EQ.'C')THEN
    GOTO 130
ENDIF
IF(CHOICE.EQ.'D')THEN
    GOTO 270
ENDIF
ENDIF
```

```

130 PRINT*, 'CALCULATE GAS 0-18 PARTIAL PRESSURE VS TIME'
PRINT*, 'ENTER INITIAL TIME, FINAL TIME, AND INCREMENTS(S)'
READ*, TI, TF, TINC
NT=INT((TF-TI)/TINC)+1
PRINT*, 'TIME(S)          0-18 ATOM FRACT.GAS          K      SUM'
WRITE(8,25) TAG,D
DO 100 I=1,NT
    SUM=0
    K=1
    T=TI+FLOAT(I)*TINC
210    SUM1=2*LAM*(1+LAM)/(1+LAM+LAM**2*ALPHA(K)**2)
    SUM2=SUM1*EXP(-4*ALPHA(K)**2*D*T/L**2)
    SUM=SUM+SUM2
    IF((SUM2/SUM).GT..00001)THEN
        K=K+1
        IF(K.GT.1000)THEN
            PRINT*, 'OVER 1000 TERMS-TERMINATED'
            GOTO 110
        ENDIF
        GOTO 210
    ENDIF
    P=P2+(P0-P2)*(1-SUM)
    PRINT*, T, P, K, SUM2
    WRITE(8,26) T, P
100 CONTINUE
    GOTO 260
270 END
SUBROUTINE AUXROOTS(LAM,ALPHA)
    DIMENSION ALPHA(1005)
    REAL LAM,L
    L=LAM
    X=2
    PI=3.141592654
    DO 100 I=1,1001
300    DX=-(X+ATAN(L*X)-PI*FLOAT(I))/(1.+L/(1+L**2*X**2))
        IF(ABS(DX/X).LT..00001)THEN
            GOTO 200
        ENDIF
        X=X+DX
        GOTO 300
200 ALPHA(I)=X
    PRINT*, I, ALPHA(I)
100 CONTINUE
    RETURN
    END

```

APPENDIX D SCANNING ELECTRON MICROGRAPHS



FIGURE D.1. Scanning  
Electron Micrograph of  
 $\text{Zr}_3\text{Sc}_4\text{O}_{12}$



FIGURE D.2. Scanning  
Electron Micrograph of  
 $\text{Zr}_3\text{Sc}_4\text{O}_{12}$



FIGURE D.3. Scanning  
Electron Micrograph of  
 $\text{Zr}_3\text{Y}_4\text{O}_{12}$



FIGURE D.4. Scanning  
Electron Micrograph of  
 $\text{Zr}_3\text{Y}_4\text{O}_{12}$

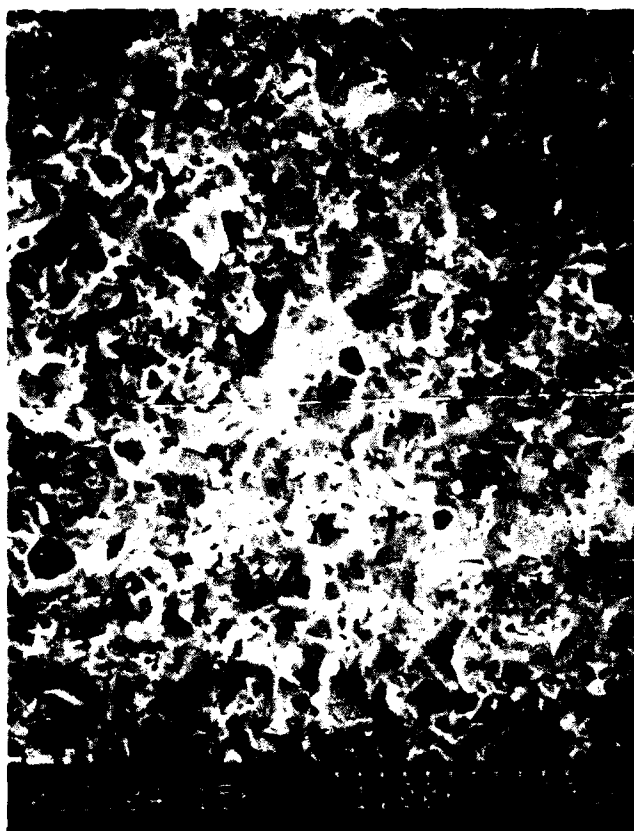


FIGURE D.5. Scanning  
Electron Micrograph of  
 $\text{Zr}_3\text{La}_4\text{O}_{12}$



FIGURE D.6. Scanning  
Electron Micrograph of  
 $\text{Zr}_3\text{La}_4\text{O}_{12}$

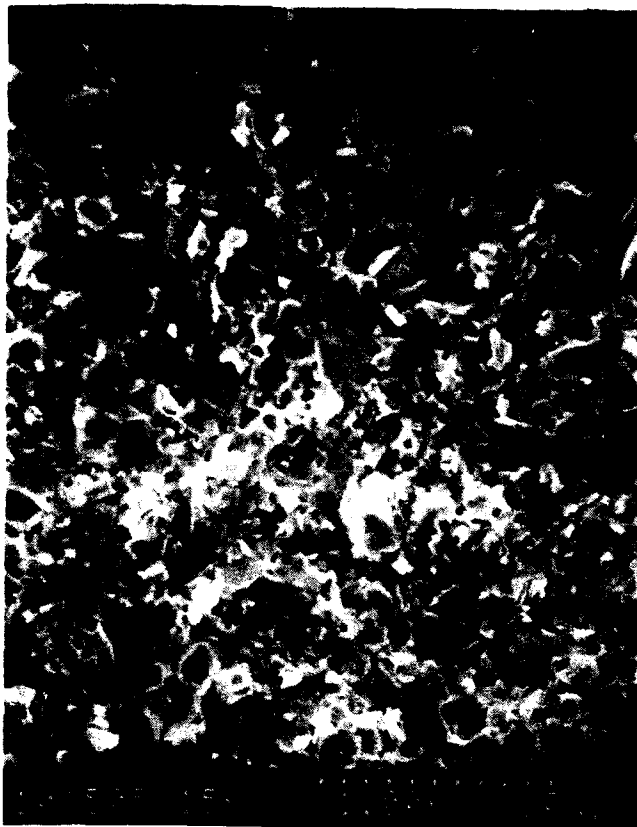


FIGURE D.7. Scanning  
Electron Micrograph of  
 $\text{Zr}_{2.98}\text{Sc}_{0.01}\text{Ta}_{0.01}\text{La}_4\text{O}_{12}$

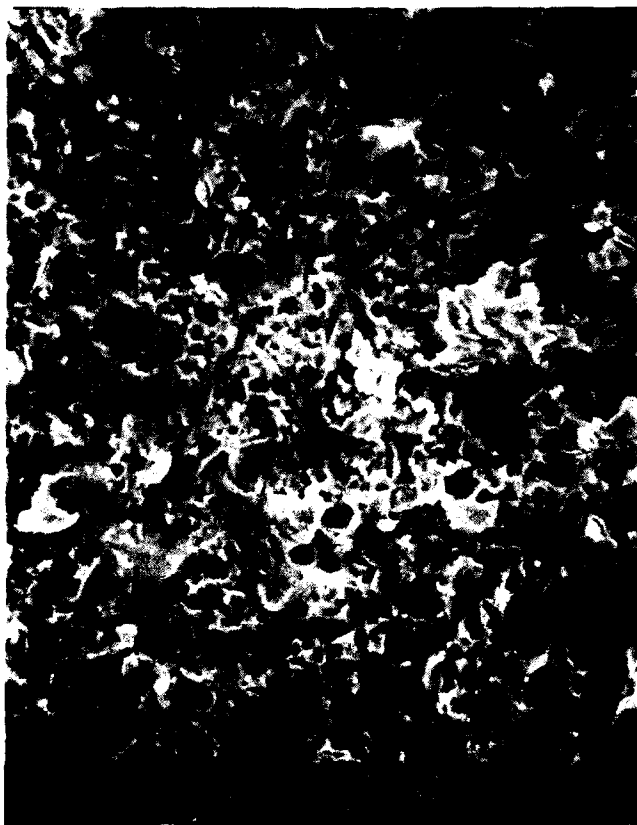


FIGURE D.8. Scanning  
Electron Micrograph of  
 $\text{Zr}_{2.9}\text{Sc}_{0.05}\text{Ta}_{0.05}\text{La}_4\text{O}_{12}$



FIGURE D.9. Scanning  
Electron Micrograph of  
 $\text{Zr}_{2.7}\text{Sc}_{0.15}\text{Ta}_{0.15}\text{La}_4\text{O}_{12}$

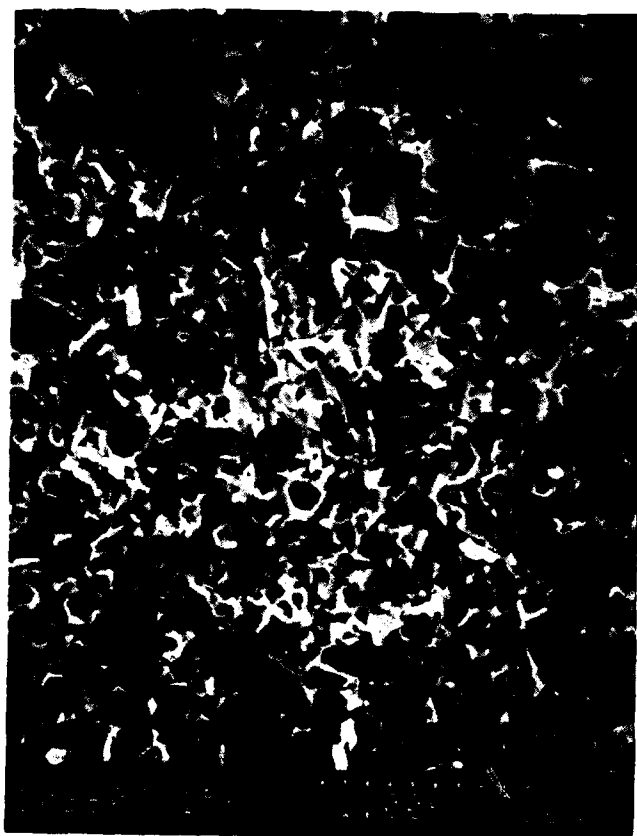


FIGURE D.10. Scanning  
Electron Micrograph of  
 $\text{Zr}_3\text{La}_{3.8}\text{Sc}_{0.2}\text{O}_{12}$



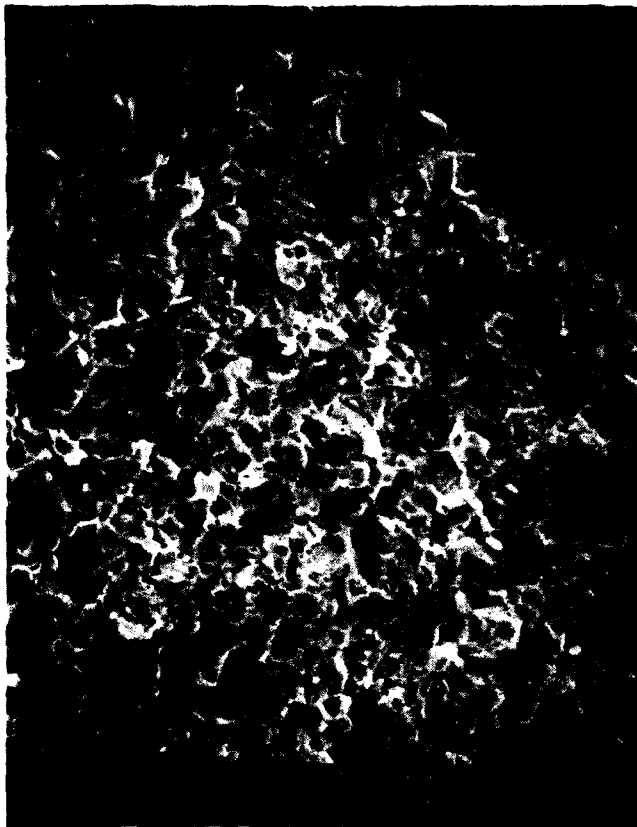


FIGURE D.11. Scanning  
Electron Micrograph of  
 $\text{Zr}_3\text{Gd}_4\text{O}_{12}$

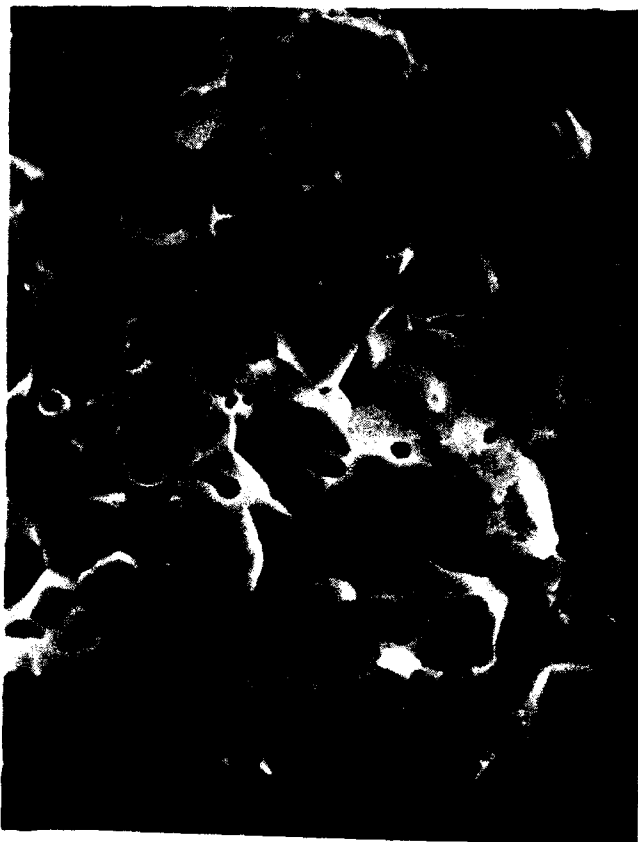
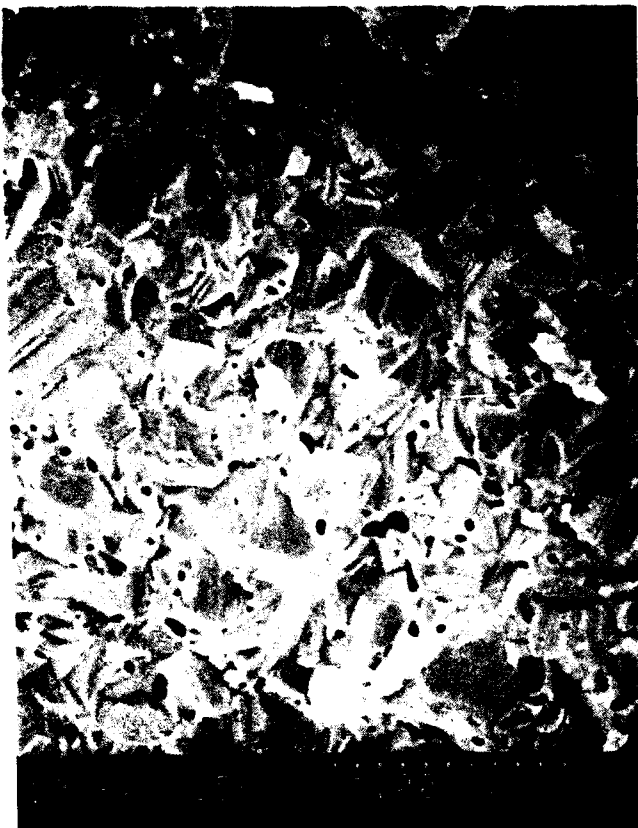
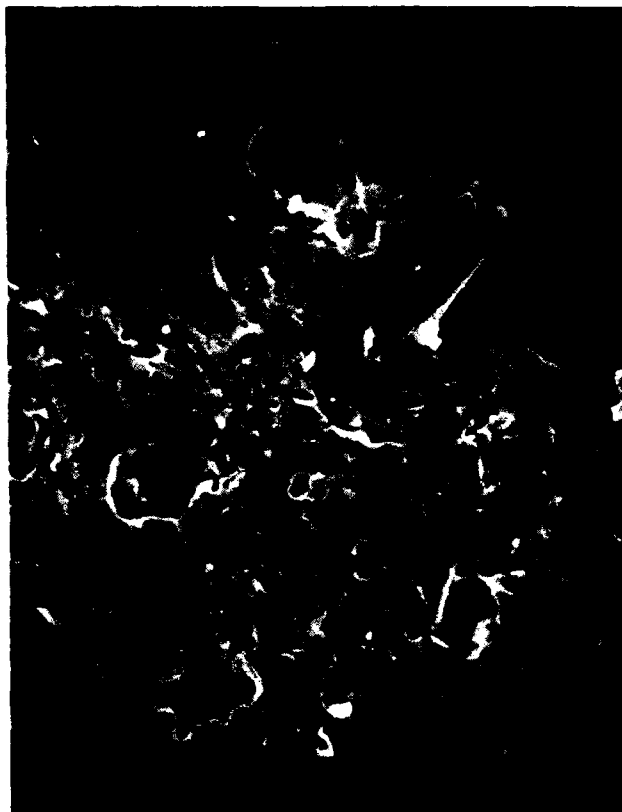


FIGURE D.12. Scanning  
Electron Micrograph of  
 $\text{Zr}_3\text{Gd}_4\text{O}_{12}$



**FIGURE D.13. Scanning  
Electron Micrograph of  
 $Y_2O_3$**



**FIGURE D.14. Scanning  
Electron Micrograph of  
Cubic Zirconia (CZ101)**

## **APPENDIX E X-RAY DIFFRACTION PATTERNS**

FN: A4008282F.NI ID: Zr3Sc4O12 FAST SCAN SCINTAG/USA  
 DATE: 9/25/90 TIME: 11:23 PT: 0.240 STEP: 0.020 WL: 1.54059

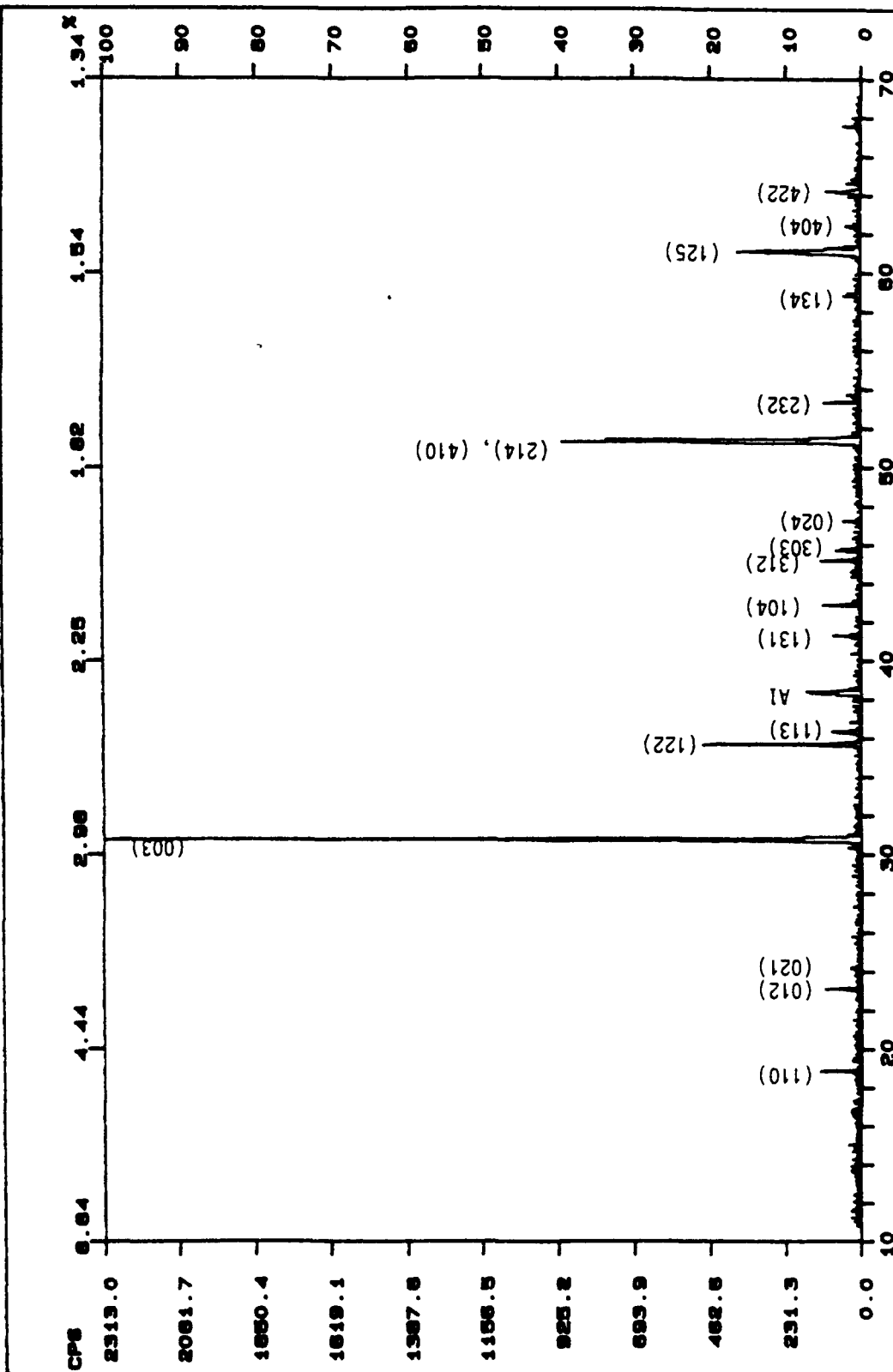


FIGURE E.1. X-ray Diffraction Pattern for  $\text{Zr}_3\text{Sc}_4\text{O}_{12}$  (hexagonal)

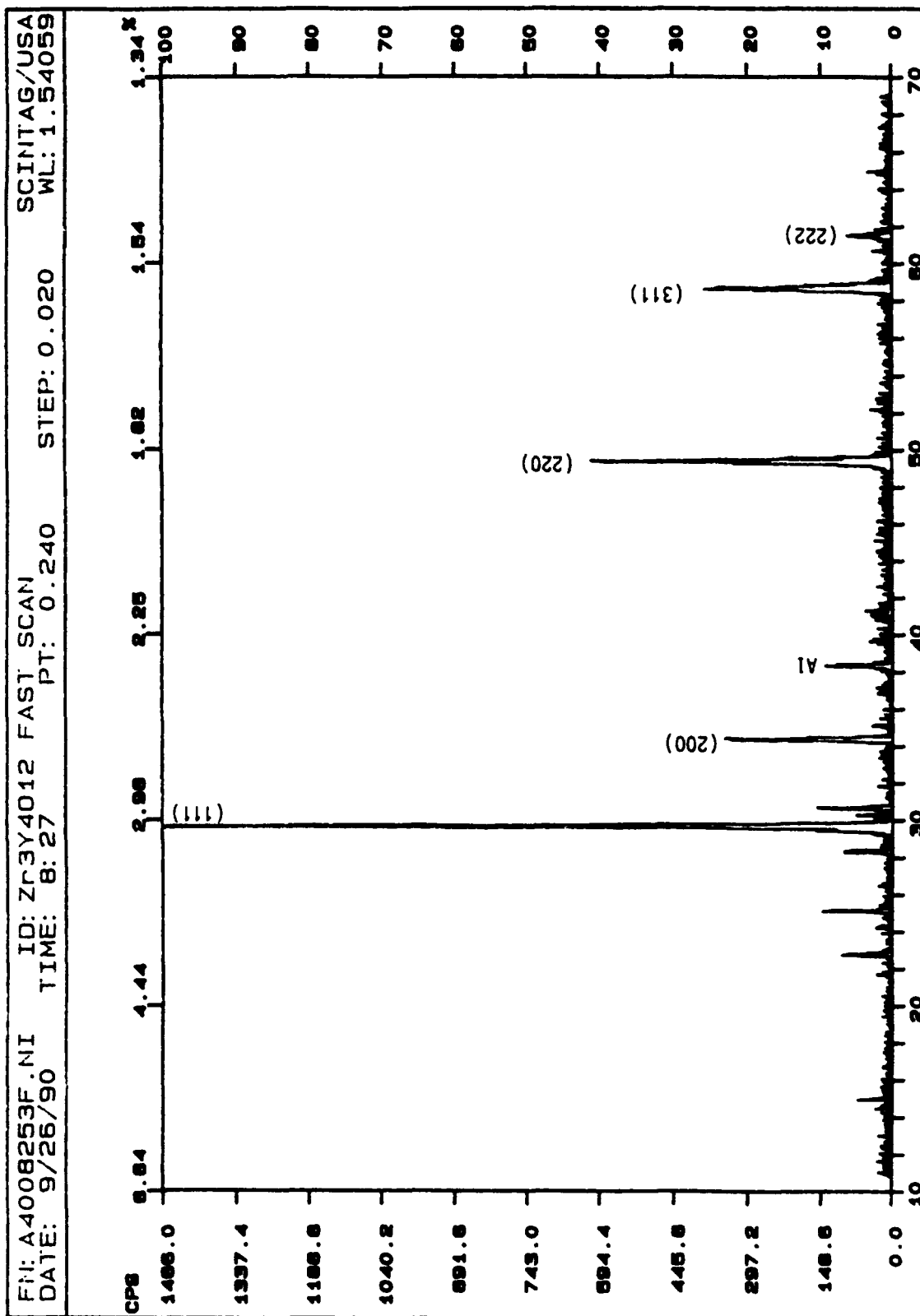


FIGURE E.2. X-ray Diffraction Pattern for  $Zr_3Y_4O_{12}$  (cubic)

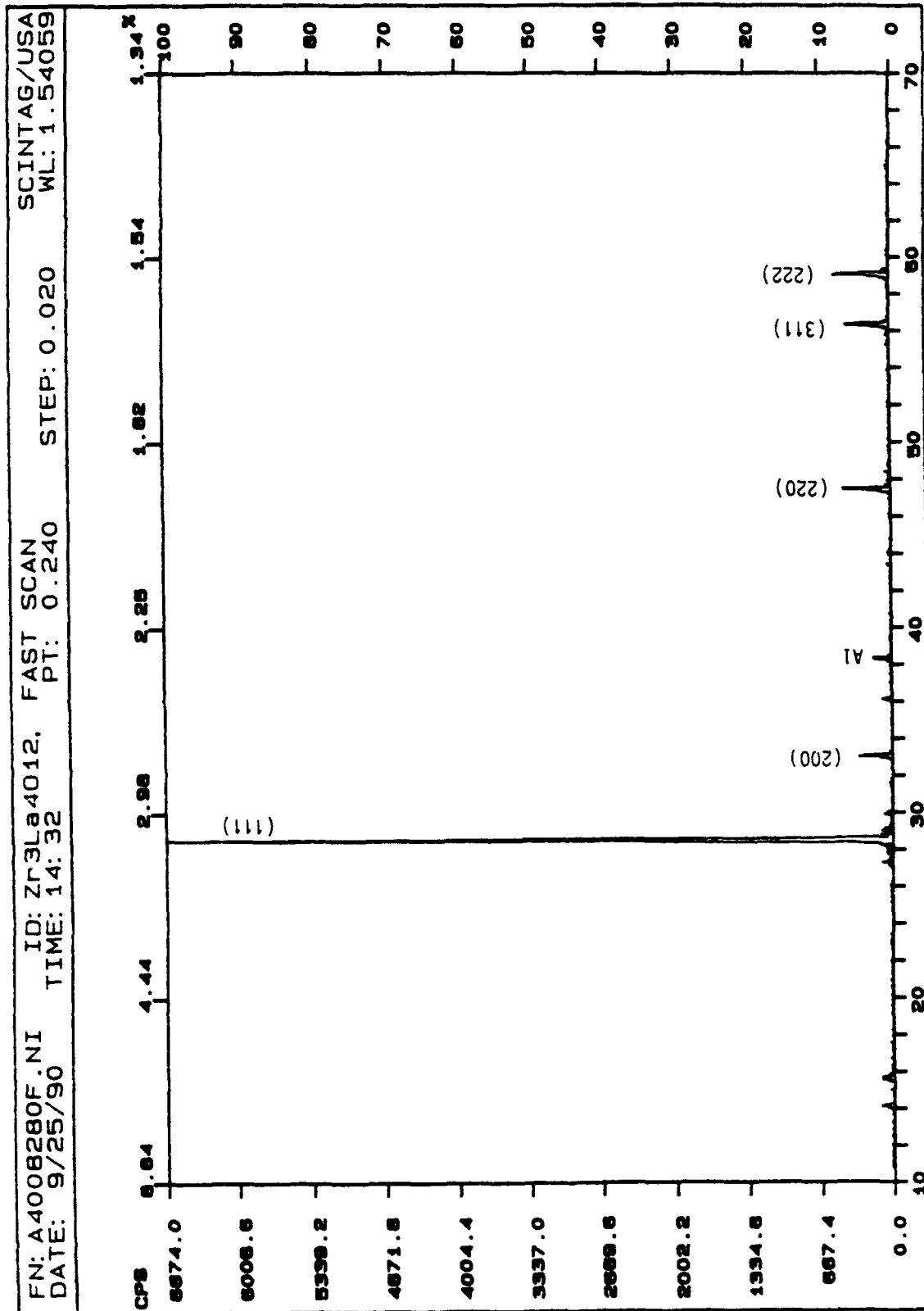


FIGURE E.3. X-ray Diffraction Pattern for Zr<sub>3</sub>La<sub>4</sub>O<sub>12</sub> (cubic)

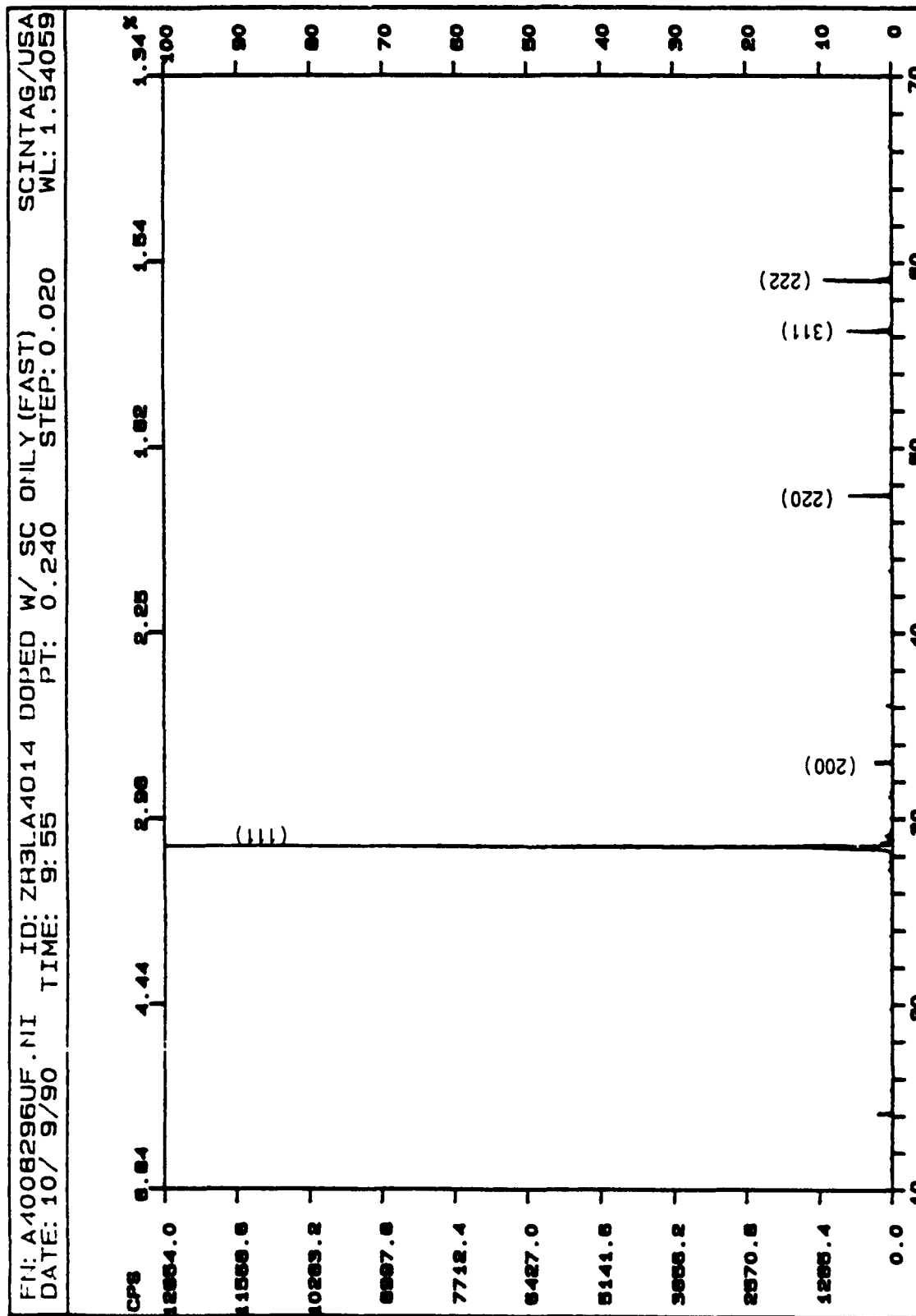


FIGURE E.4. X-ray Diffraction Pattern for  $Zr_3La_{3.8}Sc_{0.2}O_{12}$  (cubic)

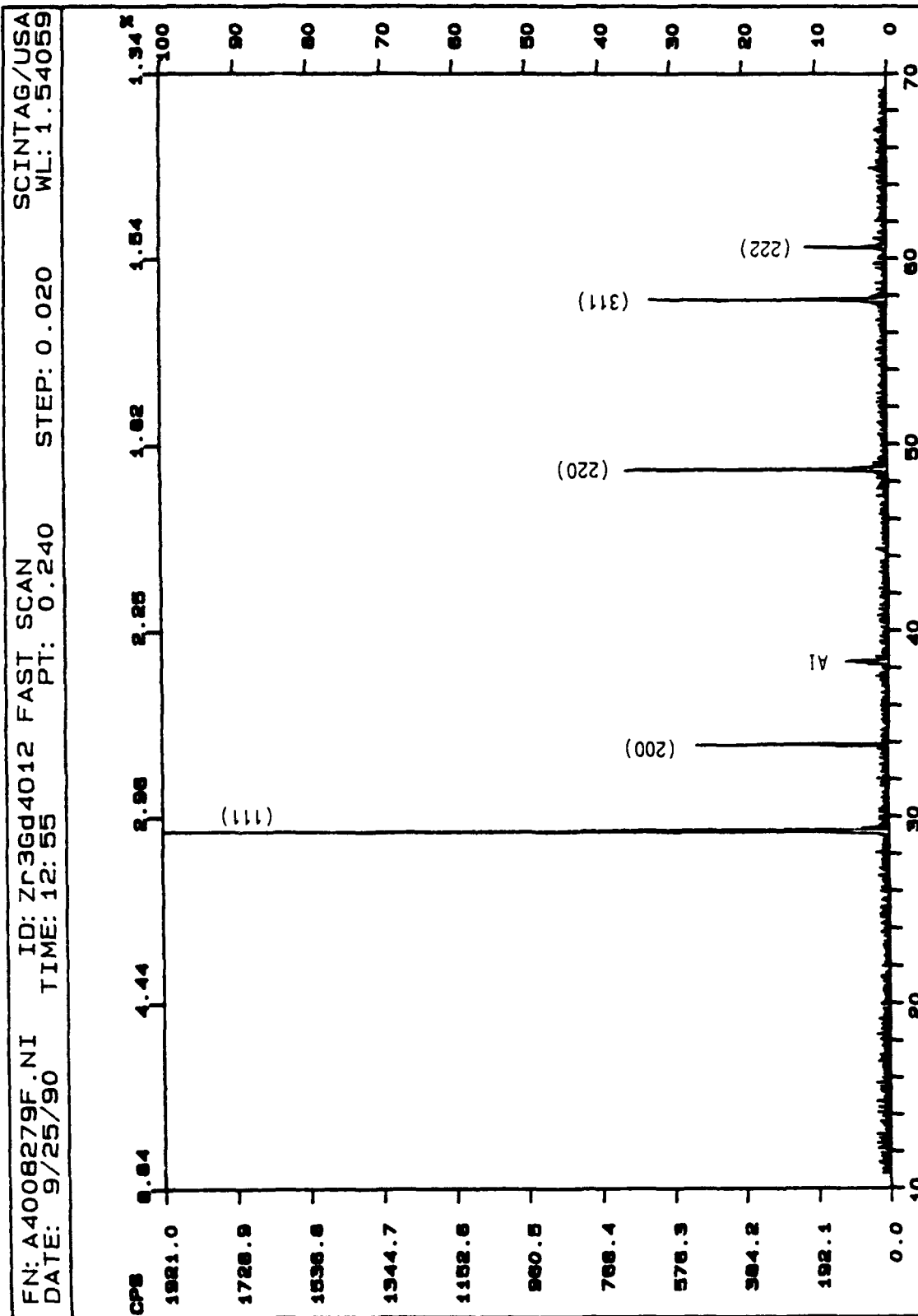


FIGURE E.5. X-ray Diffraction Pattern for  $Zr_3Gd_4O_{12}$  (cubic)



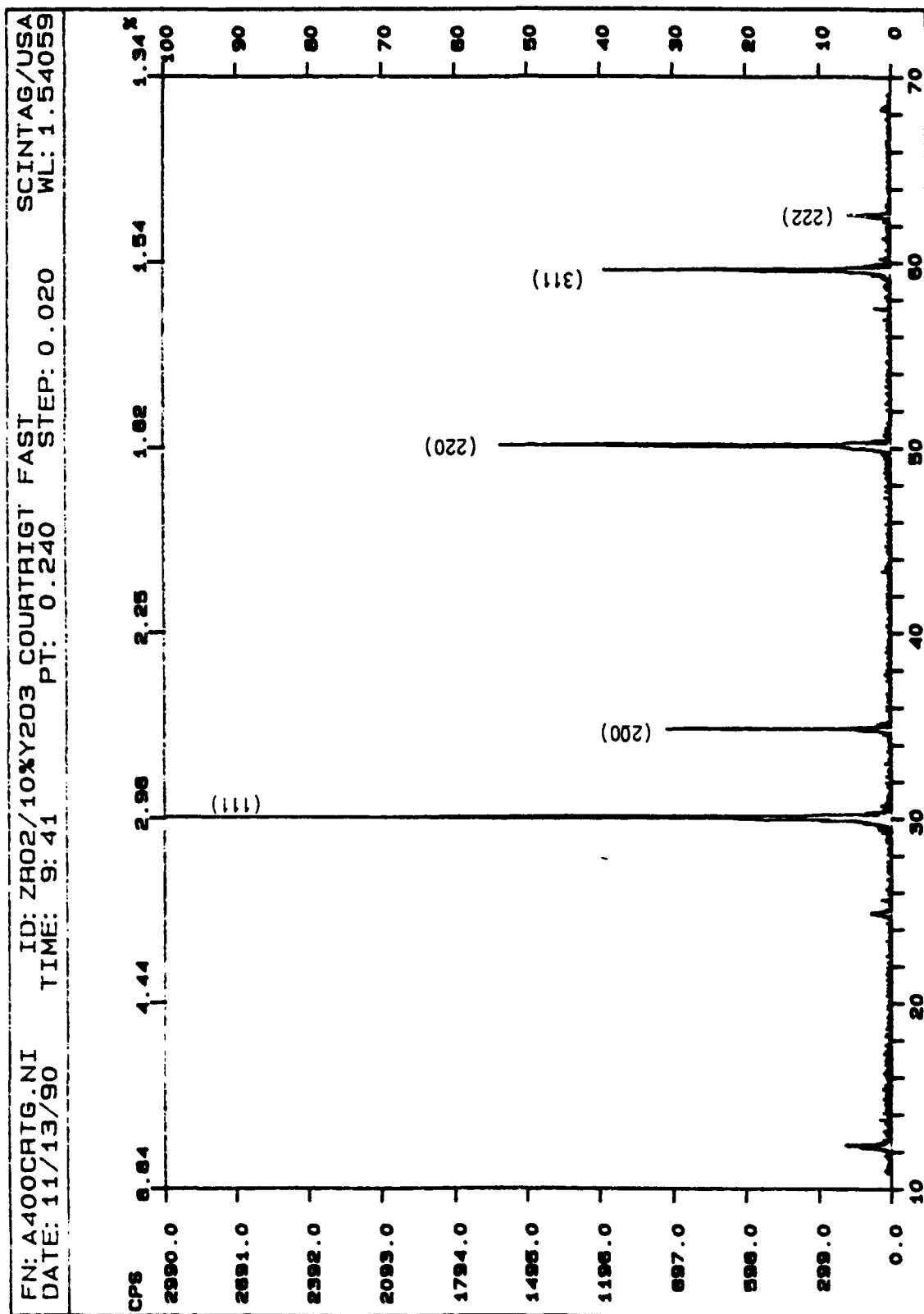


FIGURE E.6. X-ray Diffraction Pattern for CZ101 (cubic)

APPENDIX F  $[^{18}\text{O}]$  VS TIME DATA COMPARED TO THEORETICAL CURVES

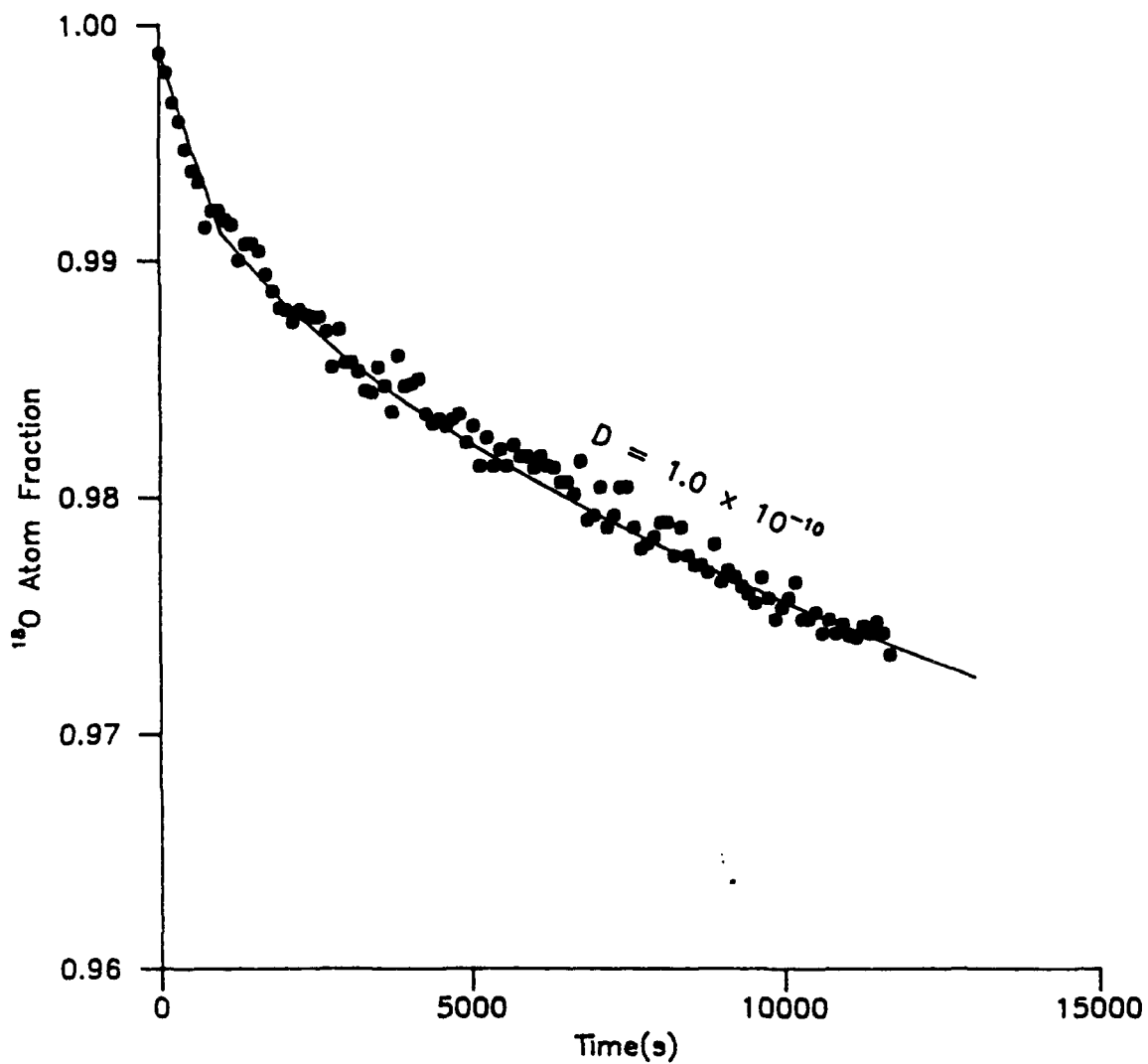


FIGURE F.1.  $[^{18}\text{O}]$  vs Time Curve for  $\text{Zr}_3\text{Sc}_4\text{O}_{12}$  at  $1135^\circ\text{C}$

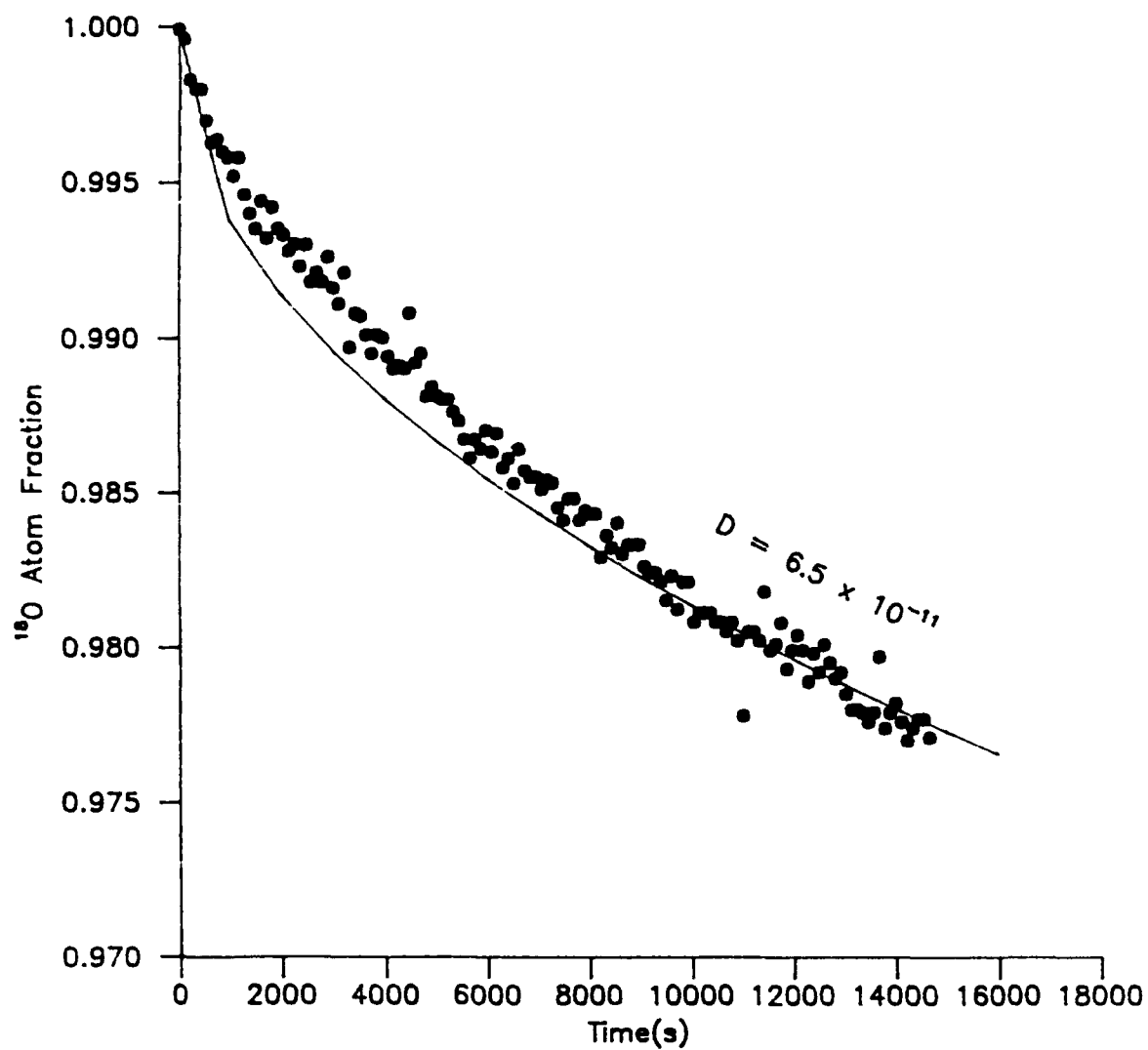


FIGURE F.2. [ $^{18}\text{O}$ ] vs Time Curve for  $\text{Zr}_3\text{Sc}_4\text{O}_{12}$  at  $1080^\circ\text{C}$

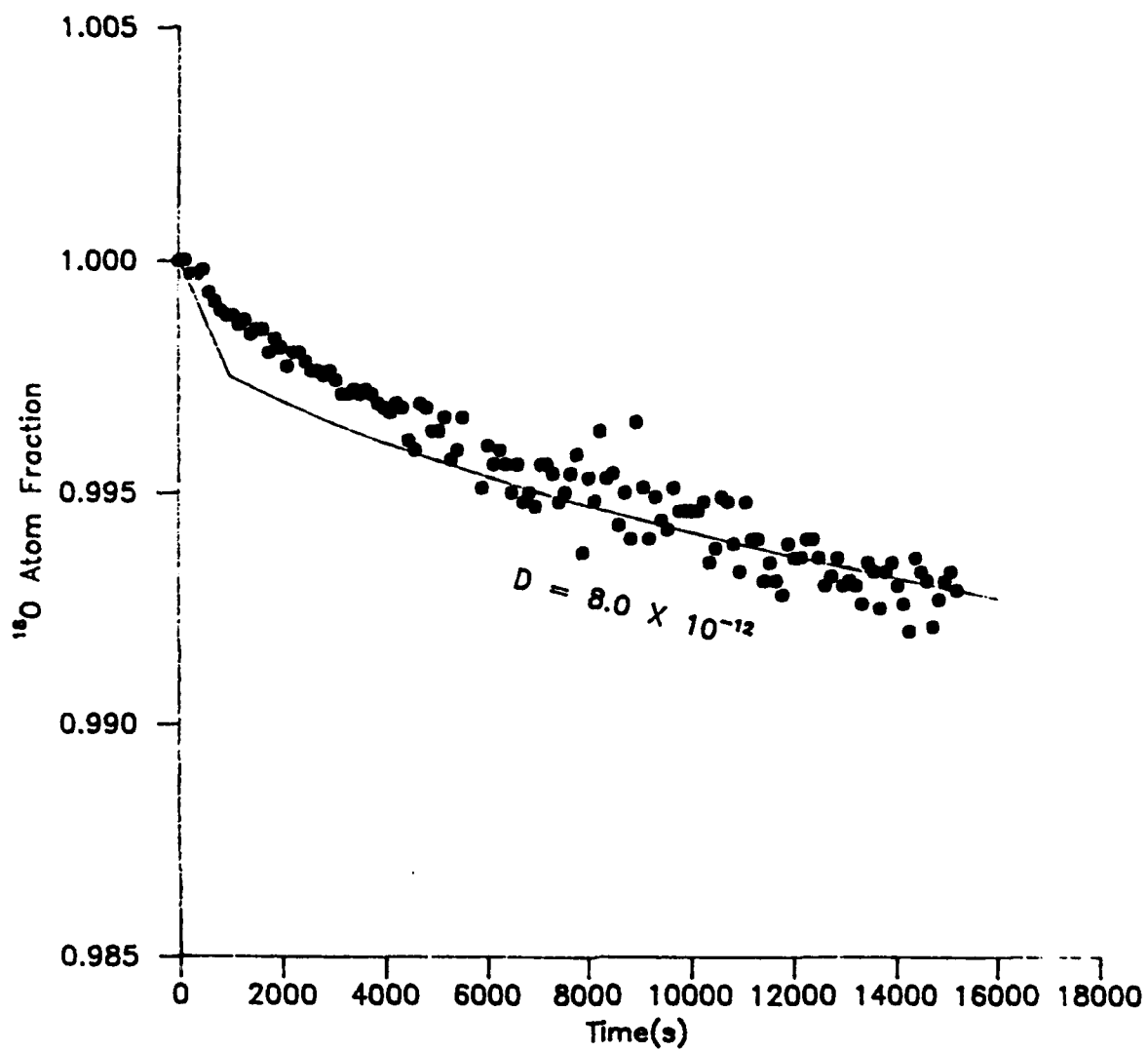


FIGURE F.3.  $[^{18}\text{O}]$  vs Time Curve for  $\text{Zr}_3\text{Sc}_4\text{O}_{12}$  at  $975^\circ\text{C}$

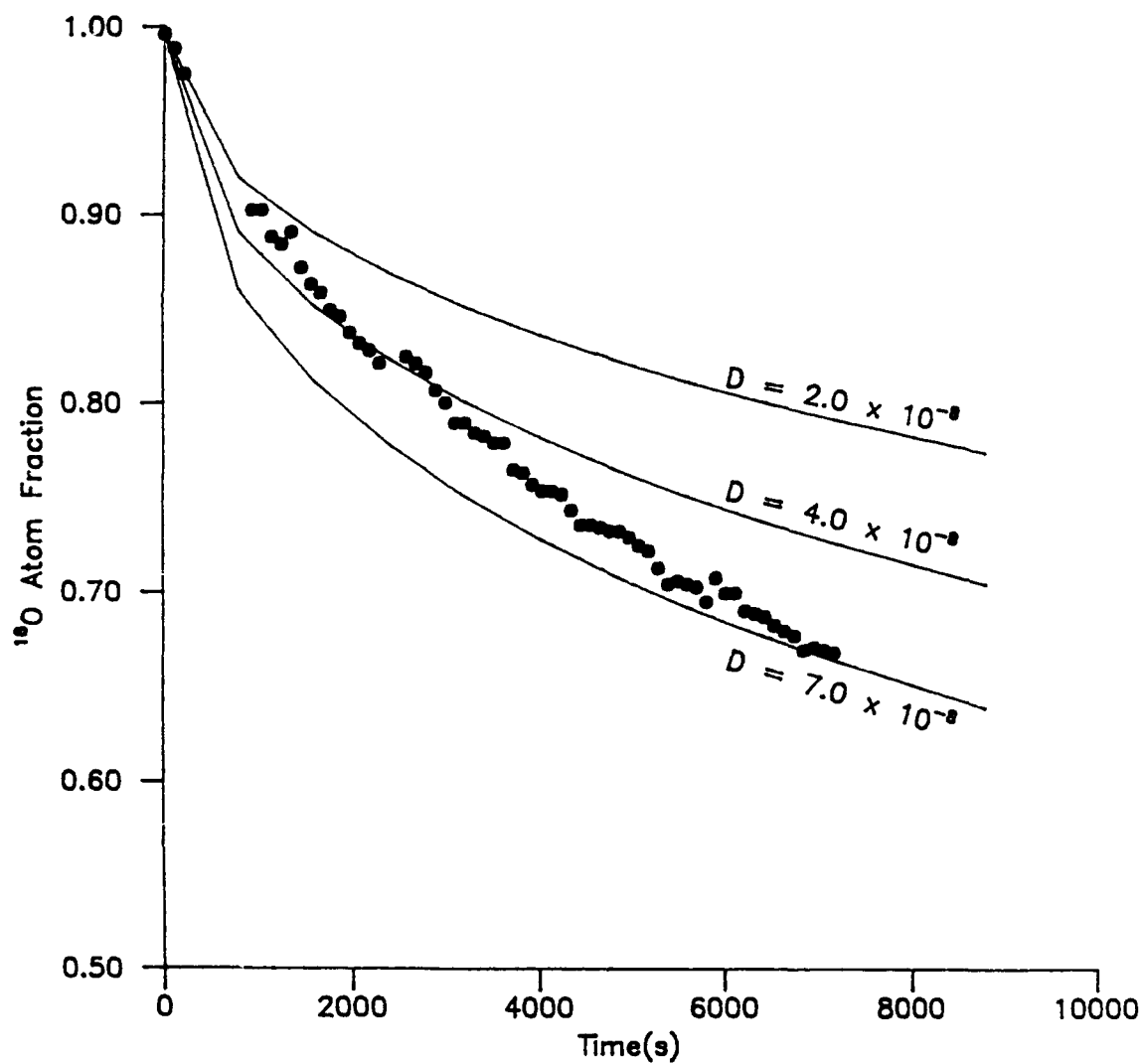


FIGURE F.4.  $[^{18}\text{O}]$  vs Time Curve for  $\text{Zr}_3\text{Y}_4\text{O}_{12}$  at  $1135^\circ\text{C}$

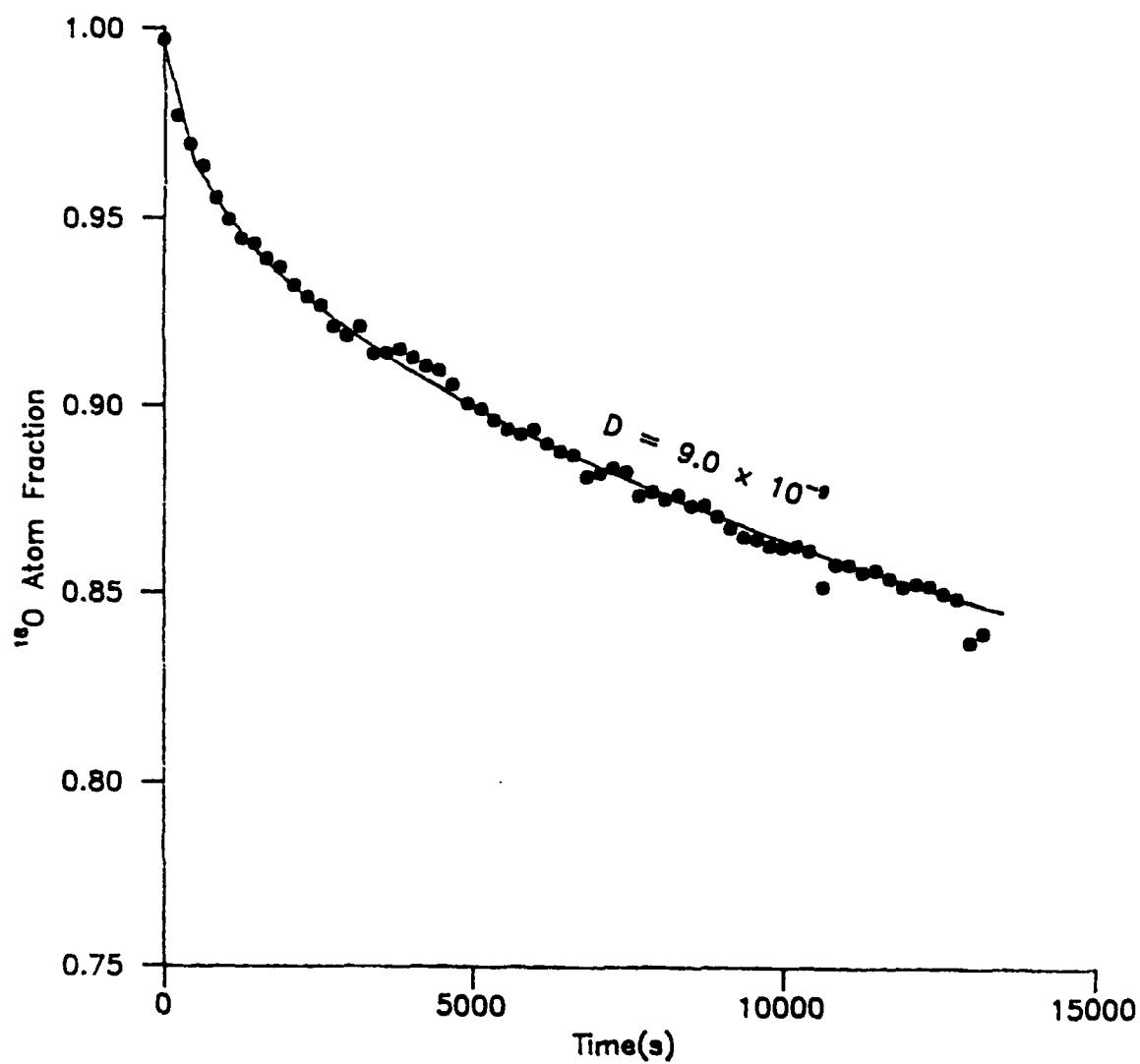


FIGURE F.5. [ $^{18}\text{O}$ ] vs Time Curve for  $\text{Zr}_3\text{La}_4\text{O}_{12}$  at  $1135^\circ\text{C}$

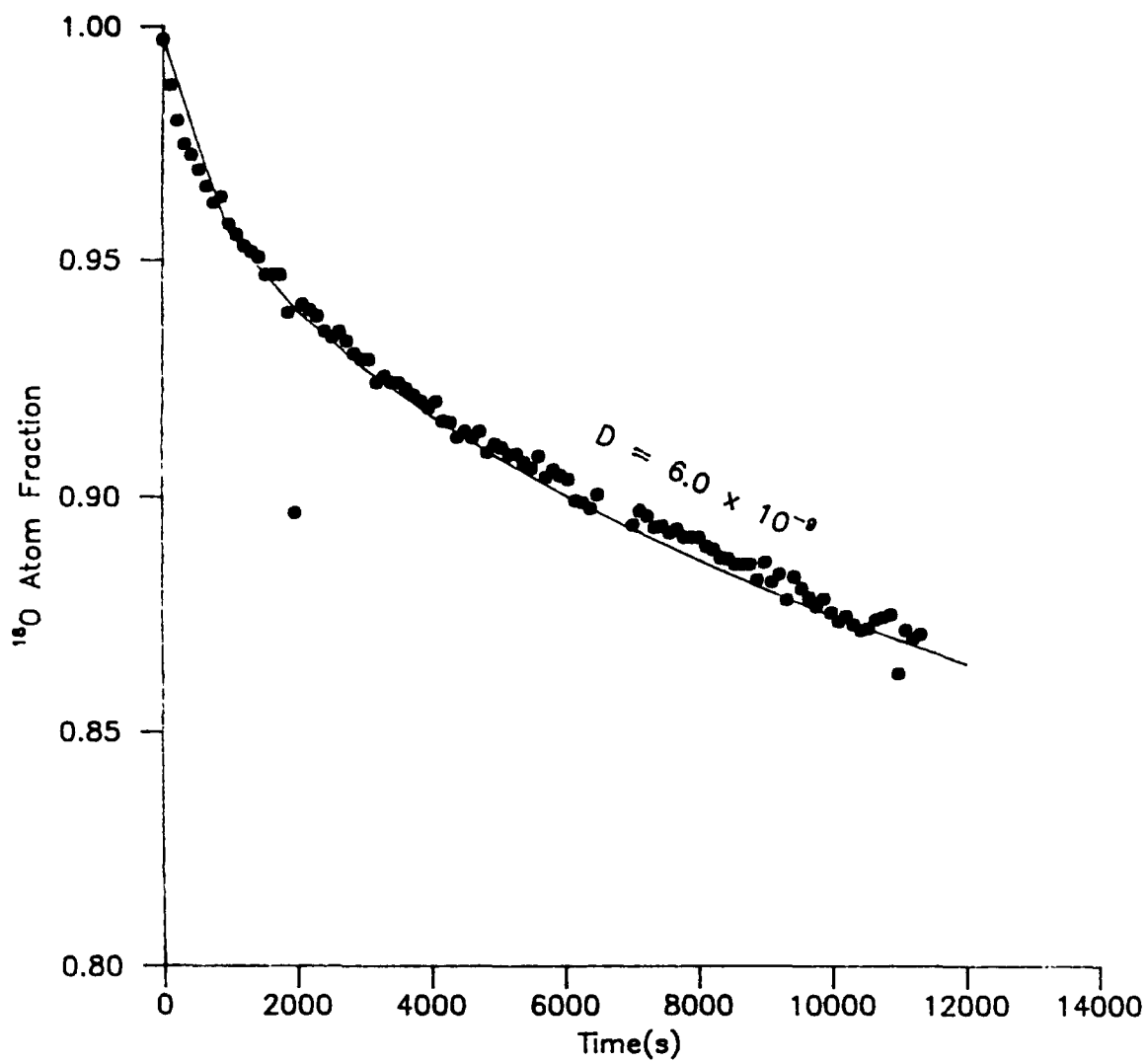


FIGURE F.6.  $[^{18}\text{O}]$  vs Time Curve for  $\text{Zr}_{2.98}\text{Sc}_{.01}\text{La}_4\text{O}_{12}$  at  $1135^\circ\text{C}$

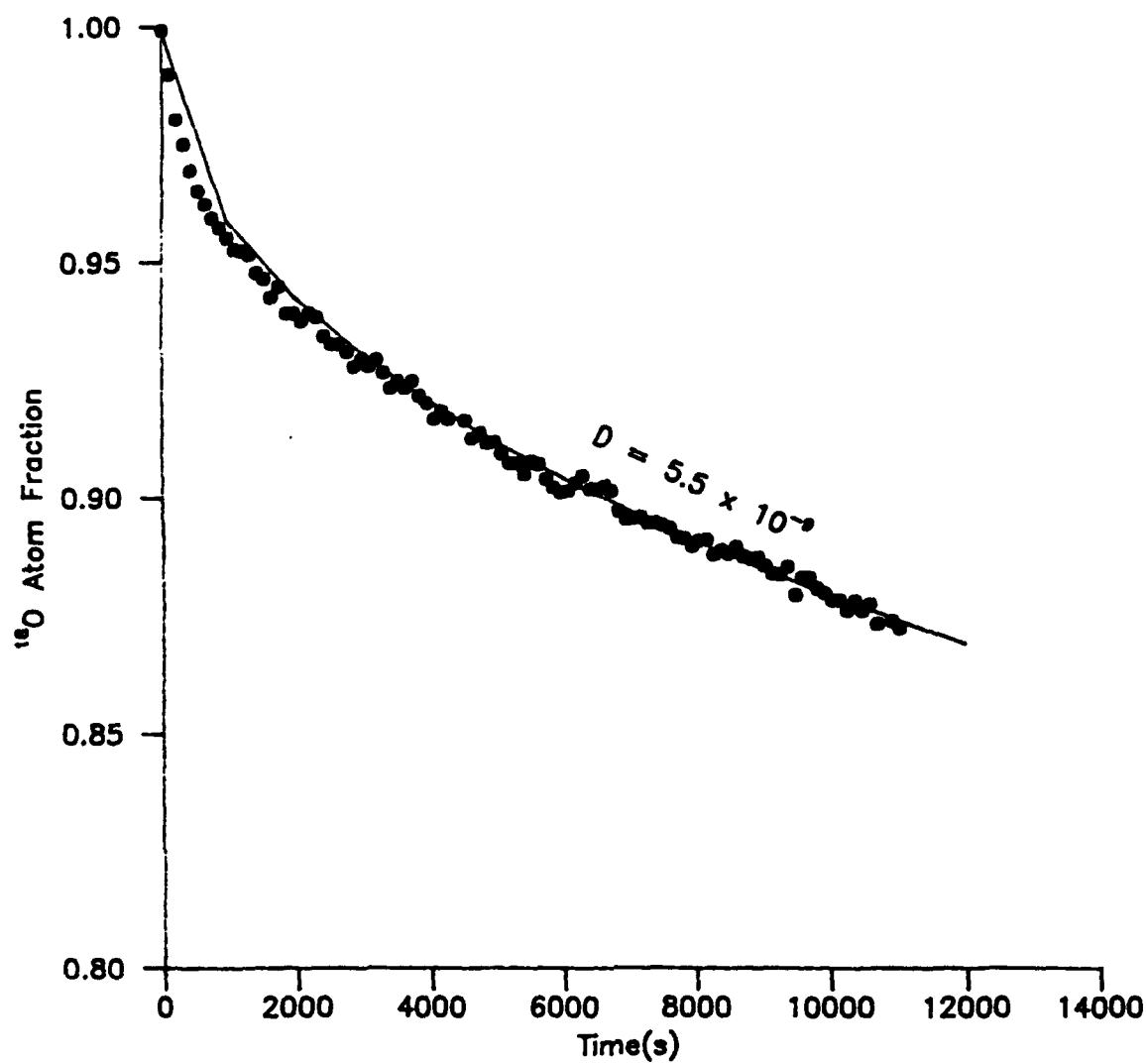


FIGURE F.7. [ $^{18}\text{O}$ ] vs Time Curve for  $\text{Zr}_{2.9}\text{Sc}_{.05}\text{Ta}_{.05}\text{La}_4\text{O}_{12}$  at  $1135^\circ\text{C}$



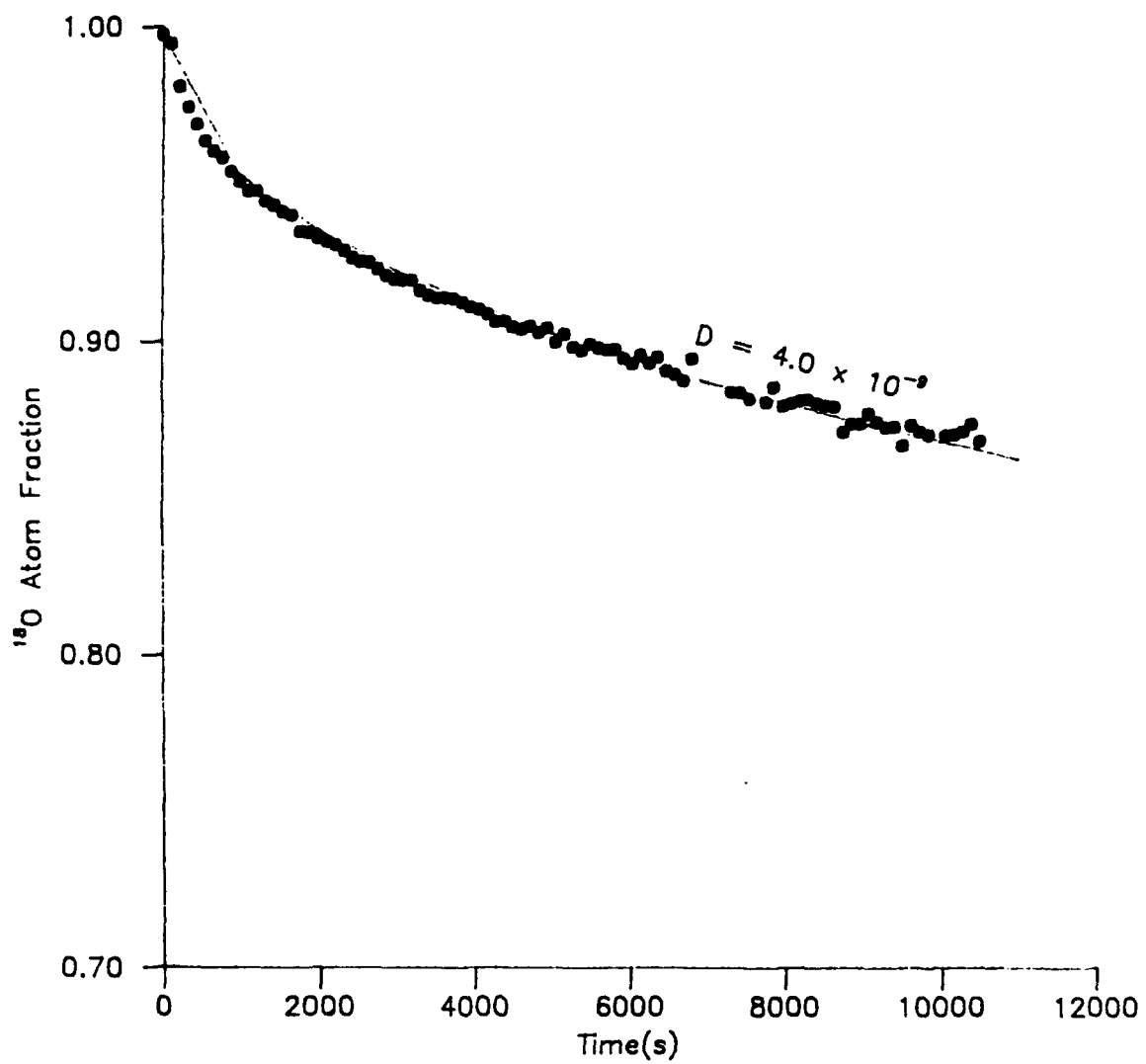


FIGURE F.8.  $[^{18}\text{O}]$  vs Time Curve for  $\text{Zr}_{2.7}\text{Sc}_{.15}\text{Ta}_{.15}\text{La}_4\text{O}_{12}$  at  $1135^\circ\text{C}$

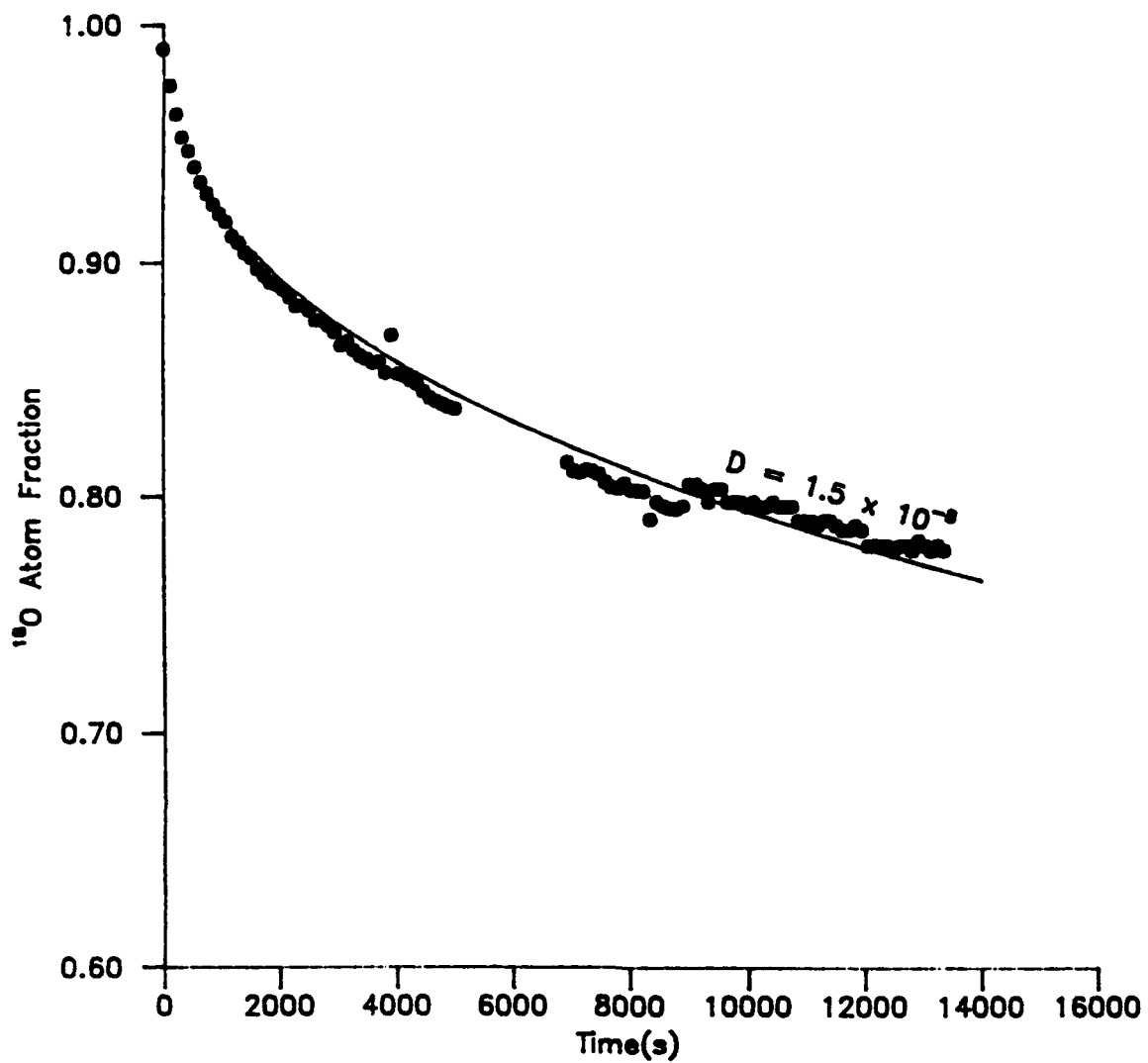


FIGURE F.9.  $[^{18}\text{O}]$  vs Time Curve for  $\text{Zr}_3\text{La}_{3.8}\text{Sc}_{.2}\text{O}_{12}$  at  $1135^\circ\text{C}$

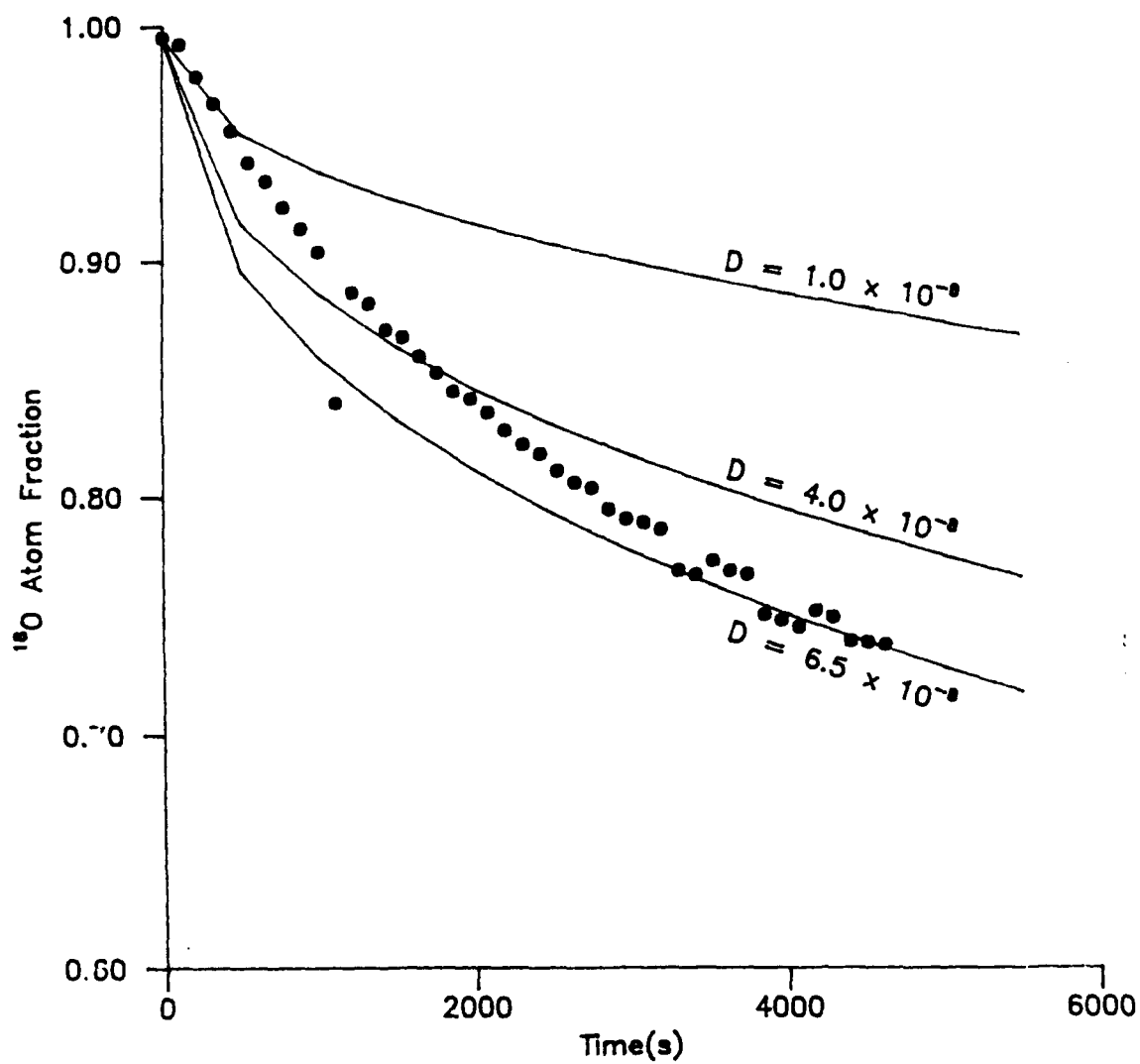


FIGURE F.10.  $[^{18}\text{O}]$  vs Time Curve for  $\text{Zr}_3\text{Gd}_4\text{O}_{12}$  at  $1135^\circ\text{C}$

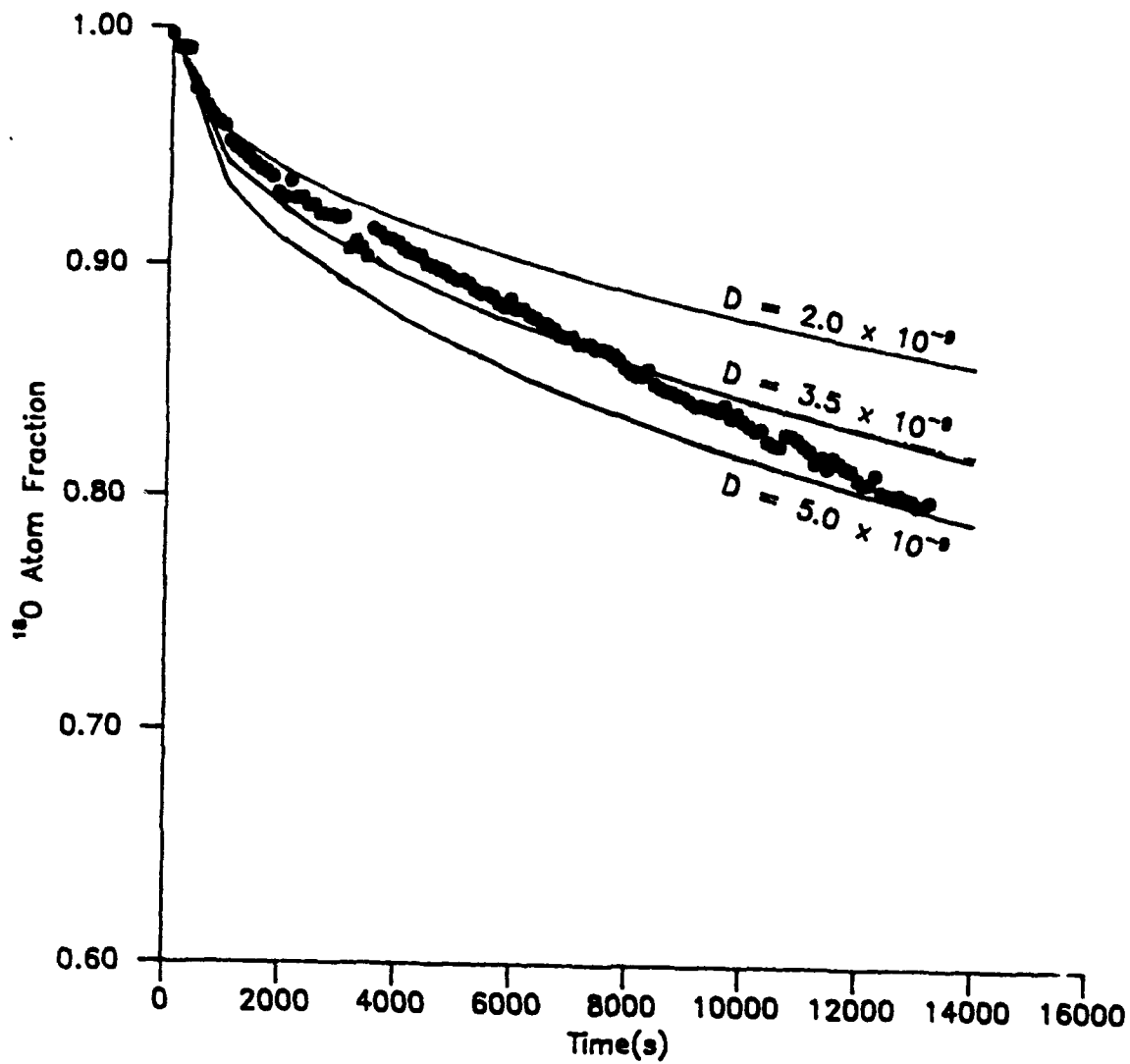


FIGURE F.11. [ $^{18}\text{O}$ ] vs Time Curve for Cubic Zirconia (CZ101)

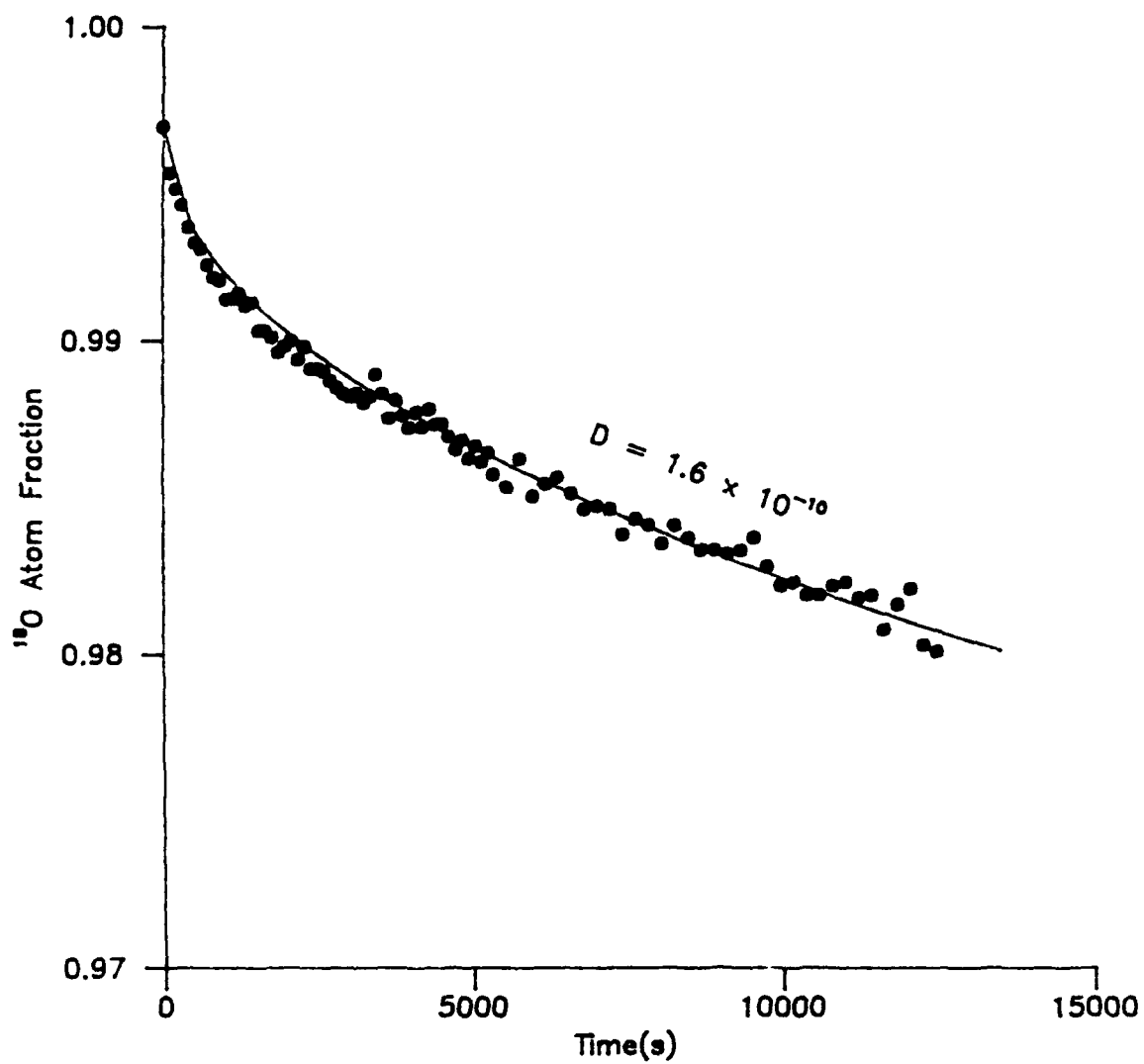


FIGURE F.12. [ $^{18}\text{O}$ ] vs Time Curve for at  $\text{Y}_2\text{O}_3$  at  $1135^\circ\text{C}$

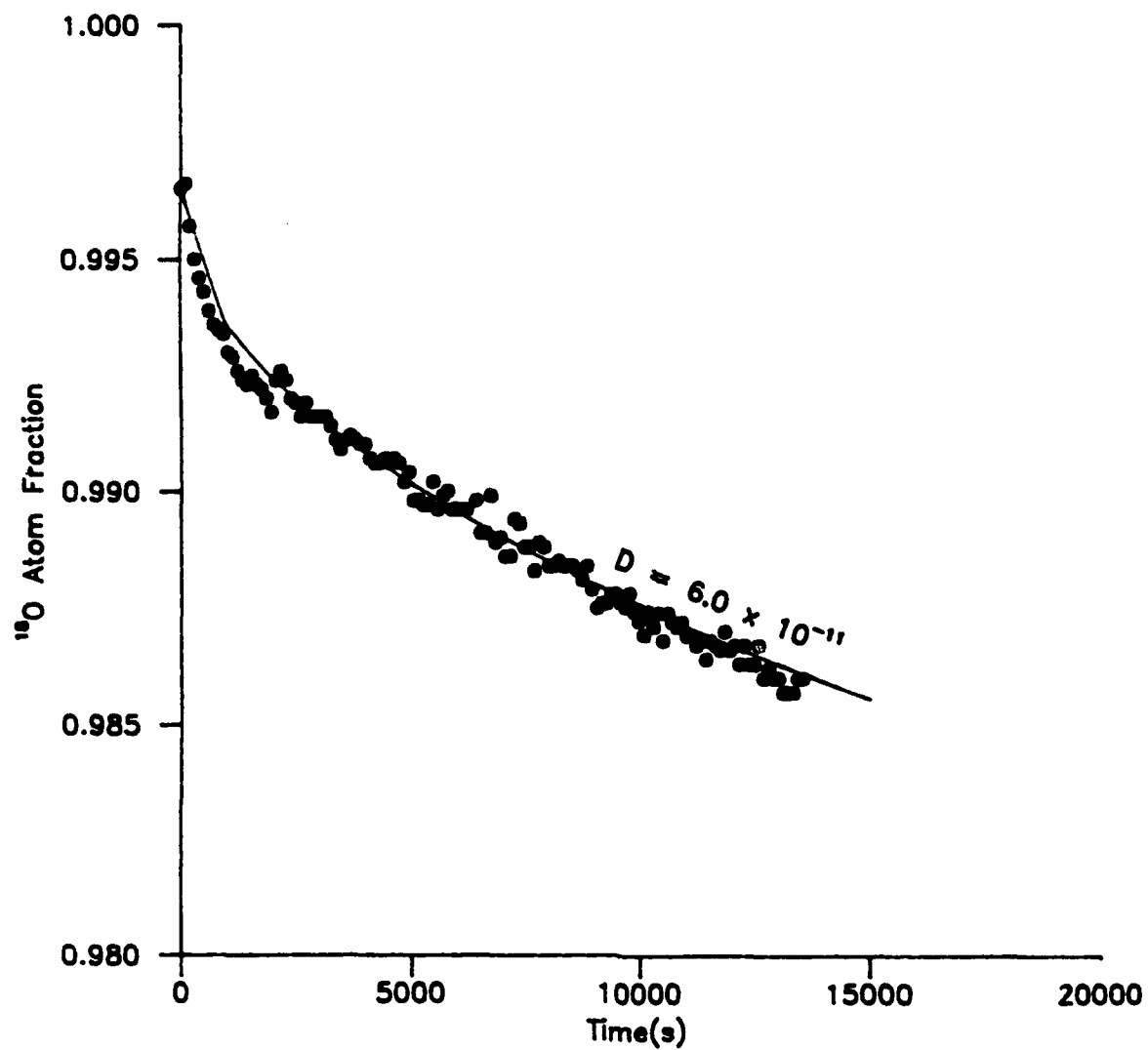


FIGURE F.13. [ $^{18}\text{O}$ ] vs Time Curve for  $\text{Y}_2\text{O}_3$  at  $1080^\circ\text{C}$

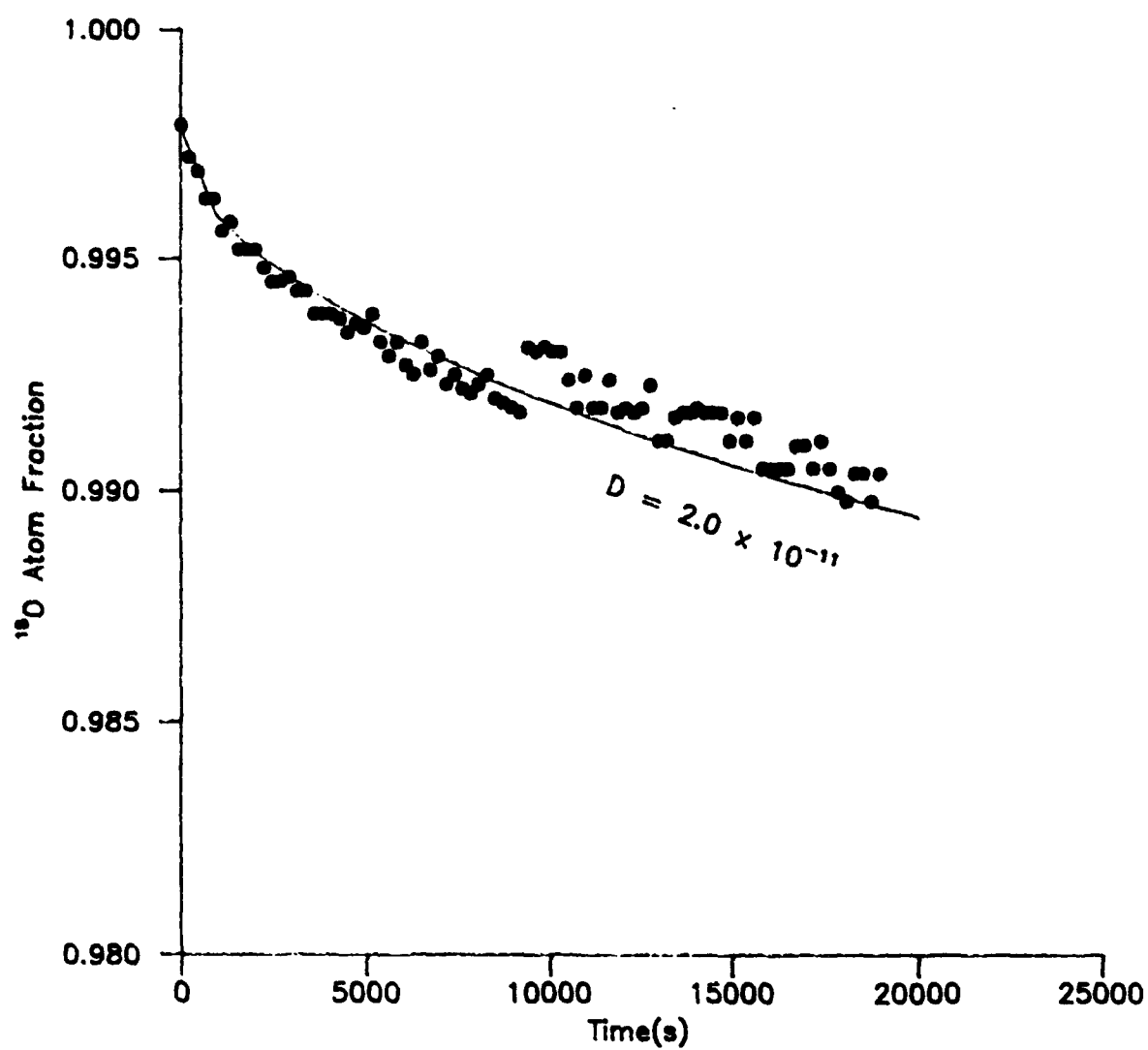


FIGURE F.14. [ $^{18}\text{O}$ ] vs Time Curve for  $\text{Y}_2\text{O}_3$  at  $975^\circ\text{C}$